2014

A Multi-Physics Computational Approach to Simulating THz Photoconductive Antennas with Comparison to Measured Data and Fabrication of Samples

Darren Ray Boyd

University of Kentucky, darrenrboyd@gmail.com

STUDENT AGREEMENT:

I represent that my thesis or dissertation and abstract are my original work. Proper attribution has been given to all outside sources. I understand that I am solely responsible for obtaining any needed copyright permissions. I have obtained needed written permission statement(s) from the owner(s) of each third-party copyrighted matter to be included in my work, allowing electronic distribution (if such use is not permitted by the fair use doctrine) which will be submitted to UKnowledge as Additional File.

I hereby grant to The University of Kentucky and its agents the irrevocable, non-exclusive, and royalty-free license to archive and make accessible my work in whole or in part in all forms of media, now or hereafter known. I agree that the document mentioned above may be made available immediately for worldwide access unless an embargo applies.

I retain all other ownership rights to the copyright of my work. I also retain the right to use in future works (such as articles or books) all or part of my work. I understand that I am free to register the copyright to my work.

REVIEW, APPROVAL AND ACCEPTANCE

The document mentioned above has been reviewed and accepted by the student's advisor, on behalf of the advisory committee, and by the Director of Graduate Studies (DGS), on behalf of the program; we verify that this is the final, approved version of the student's thesis including all changes required by the advisory committee. The undersigned agree to abide by the statements above.

Darren Ray Boyd, Student

Dr. Stephen Gedney, Major Professor

Dr. Caicheng Lu, Director of Graduate Studies

A MULTI-PHYSICS COMPUTATIONAL APPROACH TO SIMULATING THZ PHOTOCONDUCTIVE ANTENNAS WITH COMPARISON TO MEASURED DATA AND FABRICIATION OF SAMPLES

THESIS

A thesis submitted in partial fulfillment of the
requirements for the degree of Master of Science
in Electrical Engineering in the College of Engineering
at the University of Kentucky

By

Darren Ray Boyd

Lexington, Kentucky

Director: Dr. Stephen Gedney, Reese Terry Endowed Professor of Electrical Engineering

Lexington, Kentucky

2014

ABSTRACT OF THESIS

A MULTI-PHYSICS COMPUTATIONAL APPROACH TO SIMULATING THZ
PHOTOCONDUCTIVE ANTENNAS WITH COMPARISON TO MEASURED DATA
AND FABRICIATION OF SAMPLES

The frequency demands of radiating systems are moving into the terahertz band with
potential applications that include sensing, imaging, and extremely broadband
communication. One commonly used method for generating and detecting terahertz
waves is to excite a voltage-biased photoconductive antenna with an extremely short laser
pulse. The pulsed laser generates charge carriers in a photoconductive substrate which
are swept onto the metallic antenna traces to produce an electric current that radiates or
detects a terahertz band signal. Therefore, analysis of a photoconductive antenna requires
simultaneous solutions of both semiconductor physics equations (including drift-diffusion
and continuity relations) and Maxwell's equations. A multi-physics analysis scheme
based on the Discontinuous-Galerkin Finite-Element Time-Domain (DGFETD) is
presented that couples the semiconductor drift-diffusion equations with the
electromagnetic Maxwell's equations. A simple port model is discussed that efficiently
couples the two equation sets. Various photoconductive antennas were fabricated using
TiAu metallization on a GaAs substrate and the fabrication process is detailed.
Computed emission intensities are compared with measured data. Optimized antenna
designs based on the analysis are presented for a variety of antenna configurations.

KEYWORDS: Computational Electromagnetics, Photoconductive Antenna, Device
Fabrication, Semiconductor Physics, Electromagnetics

Darren R. Boyd

March 25, 2014

A MULTI-PHYSICS COMPUTATIONAL APPROACH TO SIMULATING THZ
PHOTOCONDUCTIVE ANTENNAS WITH COMPARISON TO MEASURED DATA
AND FABRICIATION OF SAMPLES

By

Darren Ray Boyd

<div style="text-align:center">

_____
Dr. Stephen Gedney
Director of Thesis

_____
Dr. Caicheng Lu
Director of Graduate Studies

_____
March 25, 2014

</div>

ACKNOWLEDGEMENTS

TABLE OF CONTENTS

LIST OF TABLES

LIST OF FIGURES

1   INTRODUCTION

1.1   Background

      With the pace of technological development and advancement in the world today, the radiating frequencies utilized by systems continue to move into new and unused ranges. One example of this is the current push of systems into the terahertz (10^{12} Hz) frequency band. These systems can be used in a wide variety of applications. Siegel [1] recounts in great detail the past and present work in terahertz technology along with its strengths and weaknesses. Historically, the terahertz band of radiation has been used primarily in astronomy, chemistry, and space science research and discovery. Now new technologies are currently being explored in sensing, imaging, and broadband communication [1]. Although terahertz systems suffer from limitations due to atmospheric absorption; the benefits of high speed communications (either in short range or space applications) and shallow penetration spectroscopy and imaging make this range of radiating systems enticing.

      Siegel [1] also states that the primary limitations on wide scale use of terahertz systems are the difficulties in creating sources. Traditional solid state electronics such as oscillators and amplifiers are limited by reactive parasitics or resistive losses. However, another method for generating and detecting terahertz waves is to excite a voltage-biased photoconductive antenna placed on a photoconductive semiconductor wafer with an extremely short laser pulse [2]. The pulsed laser generates charge carriers in the substrate which are swept onto the metallic antenna traces to produce an electric current that radiates a terahertz band signal. A similar approach is used for detection where the

voltage bias is not needed. Instead the charge carriers generated by the laser pulse are moved by the incoming signal radiated from the transmitter. This charge carrier movement similarly produces an electric current.

THz antenna structures can be designed for various application specific requirements. Since fabrication and experimental testing of these antenna designs is costly and time consuming, accurate computer simulation software is desired and can save immense resources. This is a very challenging problem since it requires a combined solution of Maxwell's equations (which represent the electromagnetic field behavior) and the drift-diffusion equations and continuity relations (which represent the semiconductor device physics).

Various methods are currently used in the computational analysis of electromagnetic fields using Maxwell's equations. For example, Method of Moment (MOM) techniques are used to solve electromagnetic boundary or volume integral equations in the frequency domain and are very useful in solving radiation and scattering problems [3]. Finite element methods (FEM) can be used to solve both frequency-domain and time-domain problems. The FEM is used to solve boundary valued electromagnetic problems using variable shaped elements allowing for highly accurate discretization of the solution domain [3].

The photoconductive antenna is a broadband device that requires a time domain solution since it is a non-linear problem [4]. Common methods for time-domain analysis are the finite-difference time-domain (FDTD), finite-element time-domain (FETD), and discontinuous Galerkin time-domain (DGTD) methods [5]. The FDTD method was initially proposed by Kane S. Yee in 1966 [6]. This method uses leapfrogged or

staggered finite differences in time and space to solve Maxwell's equations. Although it is usually straightforward and works well for various types of media, the basic Yee-algorithm is confined to a regularly spaced orthogonal grid and struggles to accommodate complex geometries and higher order accuracy [7]. The FETD is a FEM method in the time domain and, like the FDTD, requires full volume discretization. It is also based on unstructured meshing which more accurately resolves fine geometric details [7]. The FETD method is typically implicit and requires the solution of a global linear system of equations [8] which is computationally intensive. DGTD methods are also based on unstructured meshing but are locally implicit and globally explicit which makes them more efficient in time-dependent solutions [5].

In this thesis, the Discontinuous Galerkin Finite Element Time-Domain (DGFETD) method [9, 10] is presented. The DGFETD method is based on a finite element discretization of Maxwell's curl equations using field expansions via Nedelec curl-conforming basis functions instead of point based sampling [9-12]. These basis functions avoid the concern of spurious solutions and the need for penalty methods [13, 14]. Like other DGTD methods, the DGFETD also has the advantage of not requiring the solution of a global linear system of equations.

1.2 Methodology

In this thesis, a coupled solution of Maxwell's equations (describing the macroscopic relationships between the electric and magnetic fields) and the semiconductor drift-diffusion equations is formulated. Solutions for the charge carrier

3

densities and semiconductor current densities are determined using the drift-diffusion and

continuity equations and then coupled to Maxwell's equations through the current

densities at the boundary of a port implementation of the laser photogeneration in the

substrate. The resulting time-dependent differential equations are solved using the

DGFETD method. Experimental data from the literature is used to validate this method

through comparison of antenna emission intensities. Multiple antenna designs are

fabricated for further validation.

2   COMPUTATIONAL ANALYSIS

2.1   Discontinuous-Galerkin Finite Element Time Domain (DGFETD) Method

The DGFETD method is based on a finite-element discretization of the coupled Maxwell's curl equations [9, 10]

$$\nabla \times \vec{E} = -\frac{\partial}{\partial t}\bar{\bar{\mu}} \cdot \vec{H} - \bar{\bar{\sigma}}^* \cdot \vec{H} - \vec{M}, \tag{2.1}$$

$$\nabla \times \vec{H} = \frac{\partial}{\partial t}\bar{\bar{\varepsilon}} \cdot \vec{E} + \bar{\bar{\sigma}} \cdot \vec{E} + \vec{J}, \tag{2.2}$$

where the permeability, permittivity, and conductivity tensors are represented by $\bar{\bar{\mu}}$, $\bar{\bar{\varepsilon}}$, $\bar{\bar{\sigma}}^*$, and $\bar{\bar{\sigma}}$ respectively and the impressed current densities are represented by $\vec{J}$ and $\vec{M}$. The electric and magnetic fields are represented by $\vec{E}$ and $\vec{H}$. Considering the fields radiated by these current densities in a domain Ω bound by $\partial\Omega$, a finite-element discretization can be performed to subdivide this domain into non-overlapping and contiguous subdomains V_i bound by ∂V_i. Within each subdomain, the electric and magnetic field intensities are expanded using a set of hierarchical H_p - curl conforming basis functions, $f_i(\vec{r})$, weighted by unknown time-dependent coefficients, $e_i(t)$ and $h_i(t)$, such that [9, 11, 12]

$$\vec{E}(\vec{r},t) \approx \sum_{i=1}^{N_p} e_i(t) f_i(\vec{r}), \quad \vec{H}(\vec{r},t) \approx \sum_{i=1}^{N_p} h_i(t) f_i(\vec{r}). \tag{2.3}$$

A set of testing functions that span the same function space as the fields is introduced [9]. These testing functions are $\vec{T}^e$ in the electric field space and $\vec{T}^h$ in the magnetic field

5

space. The inner product of the coupled curl equations and these test functions is performed resulting in

$$\int_{V_i} \vec{T}^h \cdot \left[\frac{\partial}{\partial t} \overline{\overline{\mu}} \cdot \vec{H} + \overline{\overline{\sigma}}^* \cdot \vec{H} + \vec{M} + \nabla \times \vec{E} \right] dv = 0 \tag{2.4}$$

and

$$\int_{V_i} \vec{T}^e \cdot \left[\frac{\partial}{\partial t} \overline{\overline{\varepsilon}} \cdot \vec{E} + \overline{\overline{\sigma}} \cdot \vec{E} + \vec{J} - \nabla \times \vec{H} \right] dv = 0. \tag{2.5}$$

Assuming time independent test functions, a form of Green's first identity

$$\int_{V_i} \vec{A} \cdot \nabla \times \vec{B} dv = \int_{V_i} \vec{B} \cdot \nabla \times \vec{A} dv + \oint_{\partial V_i} \vec{A}^- \cdot \hat{n} \times \vec{B}^- ds \tag{2.6}$$

is applied. The curl term in (2.4) can then be expressed as

$$\int_{V^i} \vec{T}^h \cdot \nabla \times \vec{E} dv = \int_{V^i} \vec{E} \cdot \nabla \times \vec{T}^h dv + \oint_{\partial V_i} \vec{T}^h \cdot \left(\hat{n} \times \vec{E} \right) ds, \tag{2.7}$$

where $\hat{n}$ is the outward normal of ∂V_i [9]. By designating the electric field on the boundary ∂V_i as $\vec{E}$ (just interior) and $\vec{E}^+$ (just exterior) and assuming an impressed magnetic surface current density on the boundary of $\vec{M}_s$, the tangential electric fields must be such that

$$\hat{n} \times \left(\vec{E} - \vec{E}^+ \right) \Big|_{\partial V_i} = \vec{M}_s. \tag{2.8}$$

Due to the distributive property of the cross product over addition, this can also be written as

$$\hat{n} \times \vec{E} \Big|_{\partial V_i} = \frac{1}{2} \left(\hat{n} \times \vec{E} + \hat{n} \times \vec{E}^+ \right) \Big|_{\partial V_i} + \frac{1}{2} \vec{M}_s. \tag{2.9}$$

Using (2.9) and the relationship described in (2.7), one can show that

6

$$\int_{V_i} \vec{T}^h \cdot \nabla \times \vec{E} dv = \frac{1}{2}\int_{V_i} \vec{T}^h \cdot \nabla \times \vec{E} dv + \frac{1}{2}\int_{V_i} \vec{E} \cdot \nabla \times \vec{T}^h dv + \frac{1}{2}\oint_{\partial V_i} \vec{T} \cdot \hat{n} \times \vec{E}^+ ds + \frac{1}{2}\oint_{\partial V_i} \vec{T}^h \cdot \vec{M}_s ds. \quad (2.10)$$

Applying this to (2.4) results in

$$\int_{V_i} \left[\begin{array}{l} \dfrac{\partial}{\partial t}\vec{T}^h \cdot \overline{\overline{\mu}} \cdot \vec{H} + \vec{T}^h \cdot \overline{\overline{\sigma}}^* \cdot \vec{H} + \vec{T}^h \cdot \vec{M}_V \\ +\dfrac{1}{2}\vec{T}^h \cdot \nabla \times \vec{E} + \dfrac{1}{2}\vec{E} \cdot \nabla \times \vec{T}^h \end{array} \right] dv = -\frac{1}{2}\oint_{\partial V_i} \vec{T}^h \cdot \hat{n} \times \vec{E}^+ ds - \frac{1}{2}\oint_{\partial V_i} \vec{T}^h \cdot \vec{M}_s ds. \quad (2.11)$$

Similarly for (2.5), it can be dually written that

$$\int_{V_i} \left[\begin{array}{l} \dfrac{\partial}{\partial t}\vec{T}^e \cdot \overline{\overline{\varepsilon}} \cdot \vec{E} + \vec{T}^e \cdot \overline{\overline{\sigma}} \cdot \vec{E} + \vec{T}^e \cdot \vec{J}_V \\ -\dfrac{1}{2}\vec{T}^e \cdot \nabla \times \vec{H} - \dfrac{1}{2}\vec{H} \cdot \nabla \times \vec{T}^e \end{array} \right] dv = \frac{1}{2}\oint_{\partial V_i} \vec{T}^e \cdot \hat{n} \times \vec{H}^+ ds - \frac{1}{2}\oint_{\partial V_i} \vec{T}^e \cdot \vec{J}_s ds \quad (2.12)$$

where an impressed electric surface current density is represented by $\vec{J}_s$ and $\vec{H}^+$ is

similarly the magnetic field exterior to V_i on ∂V_i [9].

It is recognized that the fields just exterior to the volumes on the boundary are actually the fields just interior to a neighboring volume on the same boundary. Therefore, each subdomain is coupled with neighboring subdomains through the boundary integral terms in these weak forms of Maxwell's curl equations applied in each subdomain. If no impressed current densities are placed on the boundaries, these boundary integral terms also weakly enforce tangential field continuity on these boundaries [9]. This first order boundary condition weakly enforcing this continuity of the tangential fields in the absence of a source on the boundary is the central flux formulation [15].

An up-wind flux formulation is posed that uses the Robin-type transmission conditions (RTC) to scale the magnetic field boundary conditions and impressed current densities. The magnetic field boundary conditions are scaled by the effective

7

characteristic wave impedance Z^+ on ∂V^+ and Y^+ defined as $Y^+ = 1/Z^+$ [14]. Similarly, Z^- is the effective characteristic wave impedance on ∂V^- and $Y^- = 1/Z^-$ resulting in [16]:

$$Z^+\hat{n}\times\left(\vec{H}^- - \vec{H}^+\right)\Big|_{\partial V} - Z^+\vec{J}_s - \hat{n}\times\hat{n}\times\left(\vec{E}^- - \vec{E}^+\right)\Big|_{\partial V} - \hat{n}\times\vec{M}_s = 0 \qquad (2.13)$$

$$Y^+\hat{n}\times\left(\vec{E}^- - \vec{E}^+\right)\Big|_{\partial V} + Y^+\vec{M}_s + \hat{n}\times\hat{n}\times\left(\vec{H}^- - \vec{H}^+\right)\Big|_{\partial V} - \hat{n}\times\vec{J}_s = 0. \qquad (2.14)$$

For a homogeneous medium, the continuity of the normal derivative of the tangential magnetic field and the tangential derivative of the normal magnetic field across the boundary is enforced through the $\hat{n}\times\hat{n}\times\left(\vec{E}^- - \vec{E}^+\right)$ term. This weak constraint of the continuities creates a higher order boundary condition. In addition, the additional cross product on the RTC term aligns the tangential vectors and the characteristic wave impedance equates the units. With upwind flux boundary conditions, equations (2.11) and (2.12) are written as

$$\int_V \left[\frac{\partial}{\partial t}\vec{T}^h \cdot \bar{\bar{\mu}}\cdot\vec{H} + \vec{T}^h\cdot\bar{\bar{\sigma}}^*\cdot\vec{H} + \vec{T}^h\cdot\vec{M}_V + \frac{1}{2}\vec{T}^h\cdot\nabla\times\vec{E} + \frac{1}{2}\vec{E}\cdot\nabla\times\vec{T}^h\right]dv =$$
$$-\oint_{\partial V}\vec{T}^h\cdot\hat{n}\times\left(\frac{Y^+}{\bar{Y}}\vec{E}^+ + \left(\frac{Y^- - Y^+}{2\bar{Y}}\right)\vec{E} - \frac{1}{\bar{Y}}\hat{n}\times\left(\vec{H} - \vec{H}^+\right)\right)ds \qquad (2.15)$$
$$-\oint_{\partial V}\vec{T}^h\cdot\frac{1}{\bar{Y}}\left(Y^+\vec{M}_s - \hat{n}\times\vec{J}_s\right)ds$$

and

$$\int_V \left[\frac{\partial}{\partial t}\vec{T}^e\cdot\bar{\bar{\varepsilon}}\cdot\vec{E} + \vec{T}^e\cdot\bar{\bar{\sigma}}\cdot\vec{E} + \vec{T}^e\cdot\vec{J}_V - \frac{1}{2}\vec{T}^e\cdot\nabla\times\vec{H} - \frac{1}{2}\vec{H}\cdot\nabla\times\vec{T}^e\right]dv =$$
$$\oint_{\partial V}\vec{T}^e\cdot\hat{n}\times\left(\frac{Z^+}{\bar{Z}}\vec{H}^+ + \left(\frac{Z^- - Z^+}{2\bar{Z}}\right)\vec{H} + \frac{1}{\bar{Z}}\hat{n}\times\left(\vec{E} - \vec{E}^+\right)\right)ds \qquad (2.16)$$
$$-\oint_{\partial V}\vec{T}^e\cdot\frac{1}{\bar{Z}}\left(Z^+\vec{J}_s + \hat{n}\times\vec{M}_s\right)ds$$

where $\bar{Z} = Z^- + Z^+$ and $\bar{Y} = Y^- + Y^+$ [15].

Fitted polyhedral meshes are used to discretize the volume into subdomains. Again, the field intensities are expanded as in (2.3). A Galerkin formulation is achieved by spanning the same set of basis functions as test functions over the same function space. This results in the coupled difference equations

$$\frac{\partial}{\partial t}\mathbf{M}_{\mu}^{\mathbf{h,h}}\mathbf{h} + \mathbf{M}_{\sigma^*}^{\mathbf{h,h}}\mathbf{h} + \mathbf{S}^{\mathbf{h,e}}\mathbf{e} + \frac{Y^- - Y^+}{\tilde{Y}}\mathbf{F}_E^{\mathbf{h,e}^-}\mathbf{e} + \frac{1}{\tilde{Y}}\mathbf{G}^{\mathbf{h,h}^-}\mathbf{h}$$
$$= -\mathbf{T}_{M_V}^{\mathbf{h}} - \frac{Y^+}{\tilde{Y}}\mathbf{F}_E^{\mathbf{h,e}^+}\mathbf{e}^+ + \frac{1}{\tilde{Y}}\mathbf{G}^{\mathbf{h,h}^+}\mathbf{h}^+ - \frac{Y^+}{\tilde{Y}}\mathbf{T}_{M_s}^{\mathbf{h}} + \frac{1}{\tilde{Y}}\mathbf{X}_{J_s} \quad (2.17)$$

and

$$\frac{\partial}{\partial t}\mathbf{M}_{\varepsilon}^{\mathbf{e,e}}\mathbf{e} + \mathbf{M}_{\sigma}^{\mathbf{e,e}}\mathbf{e} - \mathbf{S}^{\mathbf{e,h}}\mathbf{h} - \frac{Z^- - Z^+}{\tilde{Z}}\mathbf{F}_H^{\mathbf{e,h}^-}\mathbf{h} + \frac{1}{\tilde{Z}}\mathbf{G}^{\mathbf{e,e}^-}\mathbf{e}$$
$$= -\mathbf{T}_{J_V}^{\mathbf{e}} + \frac{Z^+}{\tilde{Z}}\mathbf{F}_H^{\mathbf{e,h}^+}\mathbf{h}^+ + \frac{1}{\tilde{Z}}\mathbf{G}^{\mathbf{e,e}^+}\mathbf{e}^+ - \frac{Z^+}{\tilde{Z}}\mathbf{T}_{J_s}^{\mathbf{e}} - \frac{1}{\tilde{Z}}\mathbf{X}_{M_s} \quad (2.18)$$

derived from (2.17) and (2.18) where the superscripts denote the field test function and the field basis function types. The time-dependent coefficients vectors are **h** and **e** with the + superscript denoting exterior tangential fields. The matrices are computed as:

$$\left[\mathbf{M}_\nu\right]_{j,i} = \int_{V_i} \vec{f}_j \cdot \bar{\bar{\nu}} \cdot \vec{f}_i \, dv, \quad (2.19)$$

$$\left[\mathbf{S}\right]_{j,i} = \frac{1}{2}\int_{V_i}\left(\vec{f}_j \cdot \nabla \times \vec{f}_i + \vec{f}_i \cdot \nabla \times \vec{f}_j\right) dv, \quad (2.20)$$

$$\left[\mathbf{F}_{E/H}^+\right]_{j,k} = \frac{1}{2}\oint_{\partial V_i}\vec{f}_j \cdot \hat{n}_i \times \vec{f}_k^+ \, ds, \quad (2.21)$$

$$\left[\mathbf{T}_{J_V}\right]_j = \int_{V_i}\vec{f}_j \cdot \vec{J}_V \, dv, \text{ or } \left[\mathbf{T}_{J_s}\right]_j = \frac{1}{2}\oint_{\partial V_i}\vec{f}_j \cdot \vec{J}_s \, ds, \quad (2.22)$$

$$\left[\mathbf{G}\right]_{i,j} = \oint_{\partial V_i}\hat{n}_i \times \vec{f}_i \cdot \left(\hat{n}_j \times \vec{f}_j^+\right) ds, \quad (2.23)$$

9

$$\mathbf{X}_{J_s} = \oint_{\partial V} \vec{T}^h \cdot \hat{n} \times \vec{J}_s \, ds, \quad \mathbf{X}_{M_s} = \oint_{\partial V} \vec{T}^e \cdot \hat{n} \times \vec{M}_s \, ds \tag{2.24}$$

where $\vec{f}_i$ and $\vec{f}_j$ are the basis and testing functions for the electric and magnetic fields,

respectively, and $\overline{\overline{v}} = \overline{\overline{\mu}}, \overline{\overline{\varepsilon}}$, or $\overline{\overline{\sigma}}$. The coupled equations (2.17) and (2.18) can be

combined into the difference equation

$$\dot{\mathbf{x}} = \mathbf{A}\mathbf{x} + \mathbf{B}\mathbf{x}^+ + \mathbf{t} \tag{2.25}$$

where

$$\mathbf{x} = \begin{pmatrix} \mathbf{h} \\ \mathbf{e} \end{pmatrix}, \quad \mathbf{x}^+ = \begin{pmatrix} \mathbf{h}^+ \\ \mathbf{e}^+ \end{pmatrix}, \tag{2.26}$$

$$\mathbf{A} = \begin{pmatrix} -\mathbf{M}_\mu^{h,h^{-1}} \left(\mathbf{M}_{\sigma^*}^{h,h} + \dfrac{1}{\tilde{Y}} \mathbf{G}^{h,h^-} \right) & -\mathbf{M}_\mu^{h,h^{-1}} \left(\mathbf{S}^{h,e} + \dfrac{Y^- - Y^+}{\tilde{Y}} \mathbf{F}_E^{h,e^-} \right) \\ \mathbf{M}_\varepsilon^{e,e^{-1}} \left(\mathbf{S}^{e,h} + \dfrac{Z^- - Z^+}{\tilde{Z}} \mathbf{F}_H^{e,h^-} \right) & -\mathbf{M}_\varepsilon^{e,e^{-1}} \left(\mathbf{M}_\sigma^{e,e} + \dfrac{1}{\tilde{Z}} \mathbf{G}^{e,e^-} \right) \end{pmatrix}, \tag{2.27}$$

$$\mathbf{B} = \begin{pmatrix} \mathbf{M}_\mu^{h,h^{-1}} \dfrac{1}{\tilde{Y}} \mathbf{G}^{h,h^+} & -\mathbf{M}_\mu^{h,h^{-1}} \dfrac{Y^+}{\tilde{Y}} \mathbf{F}_E^{h,e^+} \\ \mathbf{M}_\varepsilon^{e,e^{-1}} \dfrac{Z^+}{\tilde{Z}} \mathbf{F}_H^{e,h^+} & \mathbf{M}_\varepsilon^{e,e^{-1}} \dfrac{1}{\tilde{Z}} \mathbf{G}^{e,e^+} \end{pmatrix}, \tag{2.28}$$

and

$$\mathbf{t} = \begin{pmatrix} -\mathbf{M}_\mu^{h,h^{-1}} \left(\mathbf{T}_{M_V}^h + \dfrac{Y^+}{\tilde{Y}} \mathbf{T}_{M_s}^h - \dfrac{1}{\tilde{Y}} \mathbf{X}_{J_s} \right) \\ -\mathbf{M}_\varepsilon^{e,e^{-1}} \left(\mathbf{T}_{J_V}^e + \dfrac{Z^+}{\tilde{Z}} \mathbf{T}_{J_s}^e + \dfrac{1}{\tilde{Z}} \mathbf{X}_{M_s} \right) \end{pmatrix}. \tag{2.29}$$

The first-order coupled differential equation for the fields in each sub-domain is

represented by the local difference equation (2.25). A high-order Runge-Kutta (RK)

scheme is used to simultaneously solve the difference operators in all sub-domains [9, 17,

18]. The calculations involving the inverted matrix $\mathbf{M}$ are performed using LU-factorization [9].

2.2   Semiconductor Physics Equations

In order to accurately solve photoconductive antenna problems with the DGFETD method, the effects of the interactions between the semiconductor and the laser pulse excitation must be considered. To accomplish this, the physics involved in this interaction must be added to the simulation. Consider a semiconductor with a gap between two metal traces deposited on its surface. When the substrate in the gap is illuminated with photons, the energy from the photons generates charge carriers in the substrate. If a voltage bias is applied to those traces, the generated electric field mobilizes these carriers creating current.

It is typical when evaluating the behavior of carriers over time in a substrate to begin with the continuity equations that account for the change in carrier concentrations over time. The total change in carrier concentration must equal the changes due to drift, diffusion, regeneration/combination, and other processes such as photogeneration. The combined effects of all carrier action must satisfy

$$\frac{\partial n}{\partial t} = \left.\frac{\partial n}{\partial t}\right|_{drift} + \left.\frac{\partial n}{\partial t}\right|_{diffusion} + \left.\frac{\partial n}{\partial t}\right|_{R-G} + \left.\frac{\partial n}{\partial t}\right|_{other} \tag{2.30}$$

and

$$\frac{\partial p}{\partial t} = \left.\frac{\partial p}{\partial t}\right|_{drift} + \left.\frac{\partial p}{\partial t}\right|_{diffusion} + \left.\frac{\partial p}{\partial t}\right|_{R-G} + \left.\frac{\partial p}{\partial t}\right|_{other} \tag{2.31}$$

where n and p are the concentrations of electrons and holes, respectively [19]. Defining the change in carrier concentration due to other processes as G and the change

11

in carrier concentrations due to regeneration and combination as R in addition to noting that

$$\frac{\partial n}{\partial t}\bigg|_{drift} + \frac{\partial n}{\partial t}\bigg|_{diffusion} = \frac{1}{q}\nabla \cdot \vec{J}_n \qquad (2.32)$$

and

$$\frac{\partial p}{\partial t}\bigg|_{drift} + \frac{\partial p}{\partial t}\bigg|_{diffusion} = -\frac{1}{q}\nabla \cdot \vec{J}_p \qquad (2.33)$$

where q is electric charge of an electron, $\vec{J}_n$ is the current density due to electrons, and $\vec{J}_p$ is the current density due to holes; the continuity equations can be more succinctly written as

$$\frac{\partial n}{\partial t} = \frac{1}{q}\nabla \cdot \vec{J}_n - R_n + G_n \qquad (2.34)$$

and

$$\frac{\partial p}{\partial t} = -\frac{1}{q}\nabla \cdot \vec{J}_p - R_p + G_p . \qquad (2.35)$$

Additionally, it is known that the current across the substrate is due to the drift and diffusion of the charge carriers. Therefore, the following relationships must also be satisfied:

$$\vec{J}_p = q\mu_p p\vec{E} - qD_p \nabla p \qquad (2.36)$$

and

$$\vec{J}_n = q\mu_n n\vec{E} + qD_n \nabla n \qquad (2.37)$$

where μ_n and μ_p are the carrier mobility of the electrons and holes respectively, E is the

electric field, and D_n and D_p are the carrier diffusion coefficients for the electrons and

holes respectively [19]. It is also known that the total current density

$$\vec{J} = \vec{J}_n + \vec{J}_p \tag{2.38}$$

in steady state conditions. [20]

2.3   Coupling of Equations

The semiconductor physics equations (2.34), (2.35), (2.36), and (2.37) must be coupled

with Maxwell's equations (2.1) and (2.2). In the analysis of this system, there are several

advantages to isolating the time-varying quantities. First, since the DGFETD method

uses time-integration, initial conditions in the form of steady-state sources cause an

unfavorable step discontinuity in the simulation. Isolating the time-varying quantities

avoids this. Similarly, isolating the time-varying quantities causes the intrinsic carrier

density to act as an excitation in the system. Second, by removing the static field from

the main simulation, the near-field to far-field calculation does not have to account for

this static field. Third, the time-varying fields will converge to zero over time if the time-

varying excitation is limited. Therefore, there are no non-zero terms late in the

simulation with which a PML formulation for a semiconducting material would need to

contend. Fourth, it is believed that the incorporation of doped materials may be easier

since the steady-state values are separated from the main simulation process.

Therefore, consider Maxwell's curl equations (2.1) and (2.2) as the quantities vary

with time. With no impressed magnetic or electric current density, the conductivity terms

13

neglected, and the electric current density only due to the effects of the semiconductor physics, these equations can be written as

$$\nabla \times \vec{E} = -\mu \frac{d\vec{H}}{dt} \tag{2.39}$$

and

$$\nabla \times \vec{H} = \varepsilon \frac{d\vec{E}}{dt} + \vec{J}_n + \vec{J}_p \tag{2.40}$$

where $\vec{J}_n$ and $\vec{J}_p$ are the volume current densities due to the electrons and holes, respectively. Isolating the time-varying components of the full equation set, one can write

$$\nabla \times \left[\vec{E}_0 + \vec{E}_\Delta \right] = -\mu \frac{d\left[\vec{H}_0 + \vec{H}_\Delta \right]}{dt} \tag{2.41}$$

$$\nabla \times \left[\vec{H}_0 + \vec{H}_\Delta \right] = \varepsilon \frac{d\left[\vec{E}_0 + \vec{E}_\Delta \right]}{dt} + \left[\vec{J}_{n_0} + \vec{J}_{n_\Delta} \right] + \left[\vec{J}_{p_0} + \vec{J}_{p_\Delta} \right] \tag{2.42}$$

$$q \frac{\partial \left[n_0 + n_\Delta \right]}{\partial t} = \nabla \cdot \left[\vec{J}_{n_0} + \vec{J}_{n_\Delta} \right] + qG(\mathbf{r},t) - qR(\mathbf{r},t; n_0 + n_\Delta, p_0 + p_\Delta) \tag{2.43}$$

$$q \frac{\partial \left[p_0 + p_\Delta \right]}{\partial t} = -\nabla \cdot \left[\vec{J}_{p_0} + \vec{J}_{p_\Delta} \right] + qG(\mathbf{r},t) - qR(\mathbf{r},t; n_0 + n_\Delta, p_0 + p_\Delta) \tag{2.44}$$

$$\left[\vec{J}_{n_0} + \vec{J}_{n_\Delta} \right] = q\mu_n \left[n_0 + n_\Delta \right] \left[\vec{E}_0 + \vec{E}_\Delta \right] + qD_n \nabla \left[n_0 + n_\Delta \right] \tag{2.45}$$

and

$$\left[\vec{J}_{p_0} + \vec{J}_{p_\Delta} \right] = q\mu_p \left[p_0 + p_\Delta \right] \left[\vec{E}_0 + \vec{E}_\Delta \right] - qD_p \nabla \left[p_0 + p_\Delta \right] \tag{2.46}$$

where the steady state solutions are denoted by the subscript 0 and the time-varying quantities are denoted by the subscript Δ. All time derivatives are zero in steady state so

$$\nabla \times \vec{E}_0 = 0, \tag{2.47}$$

14

$$\nabla \times \vec{H}_0 = \vec{J}_{n_0} + \vec{J}_{p_0},$$ (2.48)

$$0 = \nabla \cdot \vec{J}_{n_0} + \nabla \cdot \vec{J}_{p_0},$$ (2.49)

$$\vec{J}_{x_0} = q\mu_x x_0 \vec{E}_0 + qD_x \nabla x_0,$$ (2.50)

and

$$\vec{J}_{x_\Delta} = q\mu_x \Delta x \left[\vec{E}_0 + \vec{E}_\Delta \right] + x_0 \vec{E}_\Delta + qD_x \nabla (x_\Delta).$$ (2.51)

Note that even though $\nabla \cdot \vec{J}_{n_0} \neq 0$ and $\nabla \cdot \vec{J}_{p_0} \neq 0$ individually in general for steady-state,

the divergence of the carrier currents is balanced by the steady-state recombination rate

such that [21]

$$\nabla \cdot \vec{J}_{n_0} = qR(\mathbf{r}, t; n_0, p_0) = -\nabla \cdot \vec{J}_{p_0}.$$ (2.52)

Therefore, the time-varying set of equations can be written as

$$\nabla \times \vec{E}_\Delta = -\mu \frac{d\vec{H}_\Delta}{dt}$$ (2.53)

$$\nabla \times \vec{H}_\Delta = \varepsilon \frac{d\vec{E}_\Delta}{dt} + \vec{J}_{n_\Delta} + \vec{J}_{p_\Delta}$$ (2.54)

$$q\frac{\partial n_\Delta}{\partial t} = \nabla \cdot \vec{J}_{n_\Delta} + qG(\mathbf{r}, t) - qR(\mathbf{r}, t; n_0 + n_\Delta, p_0 + p_\Delta) + qR(\mathbf{r}, t; n_0, p_0),$$ (2.55)

$$q\frac{\partial p_\Delta}{\partial t} = -\nabla \cdot \vec{J}_{p_\Delta} + qG(\mathbf{r}, t) - qR(\mathbf{r}, t; n_0 + n_\Delta, p_0 + p_\Delta) + qR(\mathbf{r}, t; n_0, p_0),$$ (2.56)

$$J_{n_\Delta} = q\mu_n n_\Delta \left[\vec{E}_0 + \vec{E}_\Delta \right] + q\mu_n n_0 \vec{E}_\Delta + qD_n \nabla n_\Delta,$$ (2.57)

and

$$\vec{J}_{p_\Delta} = q\mu_p p_\Delta \left[\vec{E}_0 + \vec{E}_\Delta \right] + q\mu_p p_0 \vec{E}_\Delta - qD_p \nabla p_\Delta.$$ (2.58)

The implementation of this coupling is done using a port model which includes

the interaction with the semiconductor substrate and laser via a port into the field solver.

The two systems of equations are solved independently and interact through the port as shown in Figure 2.1.
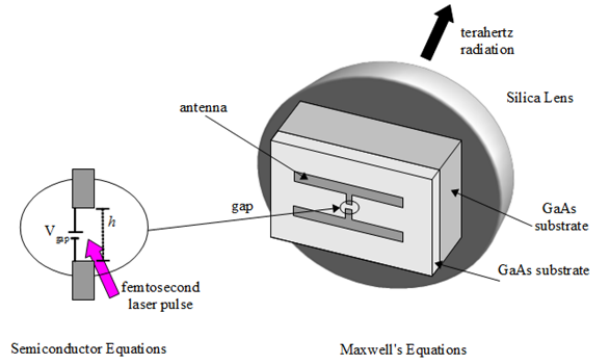
Figure 2.1 - Port Model Implementation [22]

It is assumed that the port is one-dimensional in the sense that variations in relevant quantities are only present in the length dimension of the gap from one PEC to the other, not the width dimension. According to Figure 2.1, the variations would occur in the gap length or vertical direction (y-direction) but quantities would be constant in the directions of the gap width (x direction) and thickness (z-direction). Given this assumption, one can note

$$\nabla \cdot \vec{J} = \left(\frac{d}{dy} \right) J_y \tag{2.59}$$

and

$$\nabla n = \left(\frac{dn}{dy} \right) \hat{y}, \quad \nabla p = \left(\frac{dp}{dy} \right) \hat{y}. \tag{2.60}$$

Furthermore, if it is assumed that carrier concentrations and current densities are constant along the direction of the port itself then the derivatives in the y-direction are zero so

$\nabla \cdot \vec{J} = 0$, $\nabla n = 0$, and $\nabla p = 0$. These assumptions further simplify the port

implementation.

The steady state Shockley-Reed-Hall (SRH) recombination rate is calculated as

$$R = \frac{np - n_i^2}{\tau_p (n + n_1) + \tau_n (p + p_1)}$$

(2.61)

where τ_p and τ_n are the minority carrier lifetimes of the electrons and holes, respectively.

For an undoped semiconductor with a deep level trap energy near the mid-gap,

$n_1 \approx p_1 \approx n_i$ [19, 21].

All the carrier generation is assumed to come from the light source $G = G_L$. The

steady state generation rate due to light is

$$G_L(\mathbf{r}, t) = G_0 e^{-\alpha(z - z_0)} \left[e^{-\frac{(x - x_0)^2}{\sigma_x^2} - \frac{(y - y_0)^2}{\sigma_y^2}} \right] e^{-\frac{\left[t - (z - z_0)\sqrt{\varepsilon}/c - t_0 \right]^2}{\sigma_t^2}}$$

(2.62)

where $G_0 = \dfrac{\alpha W_0}{hf}$, h is Plank's constant (6.626×10^{-34} J-s), W_0 ($J / (s\text{-}m^2)$) is the peak

optical power density, f (1/s) is the laser frequency, and α (1/m) is the absorption

coefficient of the semiconductor [19, 21, 23, 24]. The pulse spot size standard deviation

is represented by σ_x, σ_y, the pulse time standard deviation is represented by σ_t, and the

positions of the carriers are expressed by (x, y, z). For Gaussian profiles, it is assumed

that $\sigma_x = \sigma_y = \sigma_r$ [21].

3   ANTENNA DESIGN, ANALYSIS, AND VALIDATION

3.1   Base Parameters and Initial Validation

Photoconductive THz antenna structures can be designed for various application specific requirements. The bandwidth and emission intensity can be altered through variation of the dimensions and geometries of the antenna. The effects of these structural parameters are determined by evaluating various antenna structures. The results of the DGFETD computational analysis are presented and compared with expected results where possible. Consider the simple double sided dipole antenna structure presented by Miyamaru, et al. [25] such as in Figure 3.1 for initial validation.
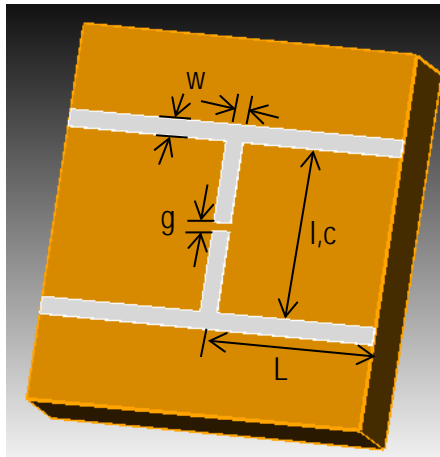
Figure 3.1 - Double Sided Full Dipole

In this example, the dipole gap length $g = 5\mu m$, the dipole trace width $w = 10\mu m$, and the dipole length l and coplanar line separation c varies from $200\mu m$ to $20\mu m$. Corresponding antenna structures are meshed using Cubit by placing PEC strips onto a

substrate as shown in Figure 3.1 and then meshing the volume for analysis. An example of a cross section of such a mesh is shown in Figure 3.2.
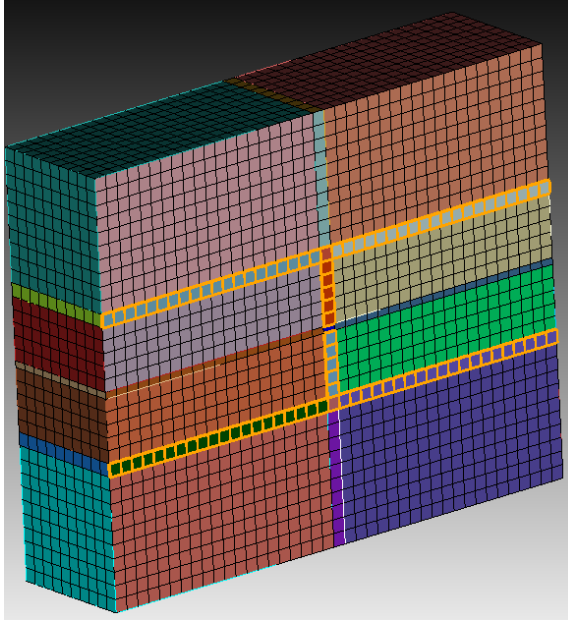
Figure 3.2 - Example Mesh Cross Section

These models are analyzed using the DGFETD method with the port implementation described above. The background is set to homogeneous isotropic loss less free space with a 1.0 relative permittivity. A bounding box of $50\mu m$ is placed around the antenna. The semiconductor material in the port placed in the dipole gap is has an electron mobility of $0.8\dfrac{m^2}{V \cdot s}$ and a hole mobility of $0.04\dfrac{m^2}{V \cdot s}$. The intrinsic carrier density is set to $2.25 \times 10^{12}\dfrac{carriers}{m^3}$ with carrier lifetimes of $0.5 \times 10^{-12}\,ps$. The temperature is set to 300 Kelvin. A static voltage of 1.0 V is applied. The semiconductor is excited by a $800nm$ laser with a uniform excitation. The laser is pulsed with a $0.1ps$

Full-Width at Half-Maximum (FWHM) pulse centered at $2\,ps$ with a peak power density

of $5 \times 10^{-3} \dfrac{W}{m^2}$. Far field calculations are conducted at an observation point in free space

perpendicular to the dipole structure $\left(\theta = 0, \varphi = 0 \right)$ and aligned with the antenna gap.

Arbitrary units (A.U.) are applied to the emission intensity results through scaling by the

wavenumber

$$k = \omega \sqrt{\mu \cdot \varepsilon} = \frac{2\pi f \sqrt{\varepsilon_r}}{c_0}. \tag{3.1}$$

This scaling is necessary because the DGFETD far field calculator normalizes the result

by the wavenumber. Therefore, this scaling effectively undoes the internal

normalization. The frequency is scaled by

$$\frac{frequency}{\sqrt{effective\_permittivity}} = \frac{f}{\sqrt{\dfrac{\varepsilon_{r_{freeSpace}} + \varepsilon_{r_{GaAs}}}{2}}} = \frac{f}{\sqrt{\dfrac{1 + 12.5}{2}}} \tag{3.2}$$

to compensate for the radiation through the substrate. The computational analysis in

Figure 3.4 agrees with the experimental results of Miyamaru, et al. [25] in Figure 3.3.
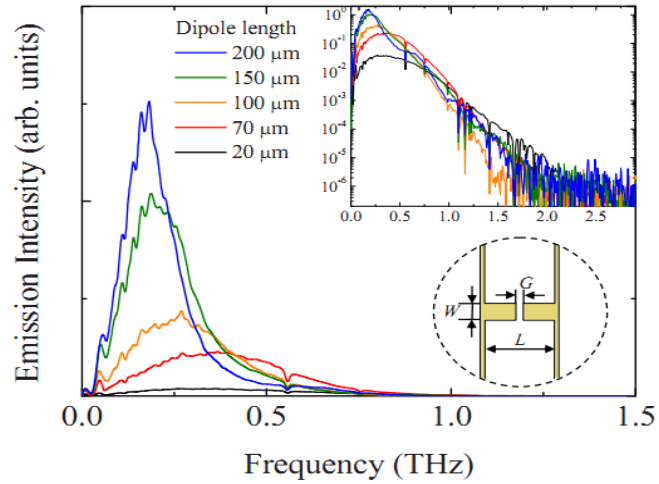
Figure 3.3 - Full Dipole Measured Emission Intensity [25]

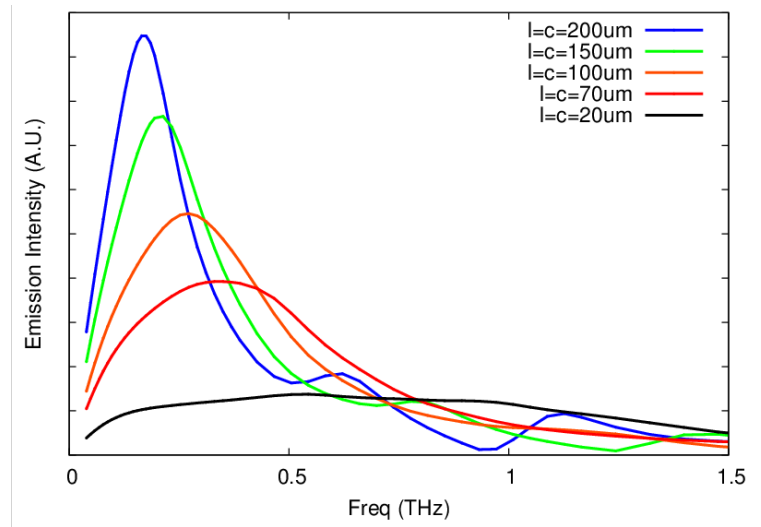Figure 3.4 – Full Dipole Computed Emission Intensity

It is observed that the resonance frequencies and bandwidth agree fairly well. However, the peak emission intensities relative to each other show a smaller decrease in peak intensity as the dipole length is reduced than expected. This might be caused by several reasons. The difference in relative peak intensities may be due to the effects of

the real world laser spot size. These simulations assume an ideal uniform excitation as opposed to an actual laser beam spot size. It is possible that a spot size much larger than the gap could cause current flow between coplanar lines or through only part of the dipole as opposed to through the entire dipole, especially at small dipole lengths. The laser spot size of this experiment is unknown.

The lower relative peak intensities may also be due to conduction losses and additional resistances introduced by the connections to testing equipment. The computational analysis does not model many of the real world additional effects of measurement taking such as equipment accuracy and imperfect transitions at device interfaces. In addition it is noted that the intensities drop off faster at higher frequencies in the experimental results than the simulations. It is theorized that this too may be due to conduction losses and resistances not currently accounted for in the simulations.

The computational analysis is conducted using a maximum mesh cell size $m = 10\mu m$ and a basis order of 2. The bases are based on the hierarchical curl-conforming basis functions developed by J. P. Webb [12] for tetrahedron that have been developed for hexahedron [9]. The mesh cell size and basis order parameters are maximized for minimal error with the shortest simulation time. A study was conducted varying the maximum mesh cell size and basis order for the full dipole length of $100\mu m$ case with results plotted in Figure 3.5.
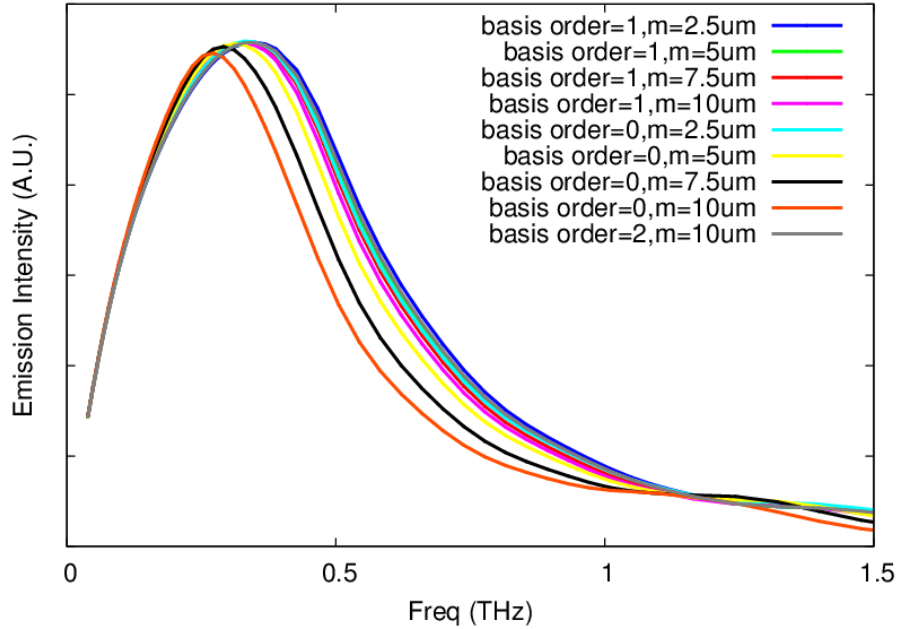
Figure 3.5 - Mesh Cell Size vs. Basis Order

It is more insightful to examine the relative error of the results as shown in Table 3.1.

The simulation with basis order of 1 and maximum cell size of $2.5\mu m$ is used as a

reference value for the relative error calculations such that

$$relative\_error = \frac{1}{N}\cdot\sum_{n=0}^{N-1}\frac{\left|reference_n - test_n\right|}{\left|reference_n\right|}\cdot100\% \qquad (3.3)$$

where N is the number of data points and *test* is the data under analysis.

Table 3.1- Basis Order/Cell Size Relative Errors

Basis Order	Maximum Cell Size	Relative Error
1	$2.5\,\mu m$	Reference
1	$5\,\mu m$	2.5%
1	$7.5\,\mu m$	5.7%
1	$10\,\mu m$	8.0%
0	$2.5\,\mu m$	4.7%
0	$5\,\mu m$	12.8%
0	$7.5\,\mu m$	17.5%
0	$10\,\mu m$	22.1%
2	$10\,\mu m$	2.0%

It is noted that using a maximum mesh cell size of $5\,\mu m$ and a basis order of 1 nearly

reduces the error in half from the mesh cell size of $2.5\,\mu m$, basis order $= 0$ case.

Furthermore, the basis order $= 2$ and maximum mesh cell size of $10\,\mu m$ resulted in a

slightly better relative error. This basis order of 2 with a maximum mesh cell size of

$10\,\mu m$ resulted in best combination of lowest error and simulation time.

The computational analysis is conducted with coplanar lines $L = 200\,\mu m$ long on

each side of the dipole (for double sided designs). It is determined that this is sufficient

for stable analysis results while keeping the problem space as small as possible to

minimize simulation time. This value of $200\,\mu m$ is determined by simulating the same

double sided full dipole antenna with a coplanar line separation of $100\mu m$ with varying

coplanar line lengths. Figure 3.6 shows the results with a slight difference in lengths of

$100\mu m$ and $200\mu m$ but negligible difference between $200\mu m$ and $400\mu m$.
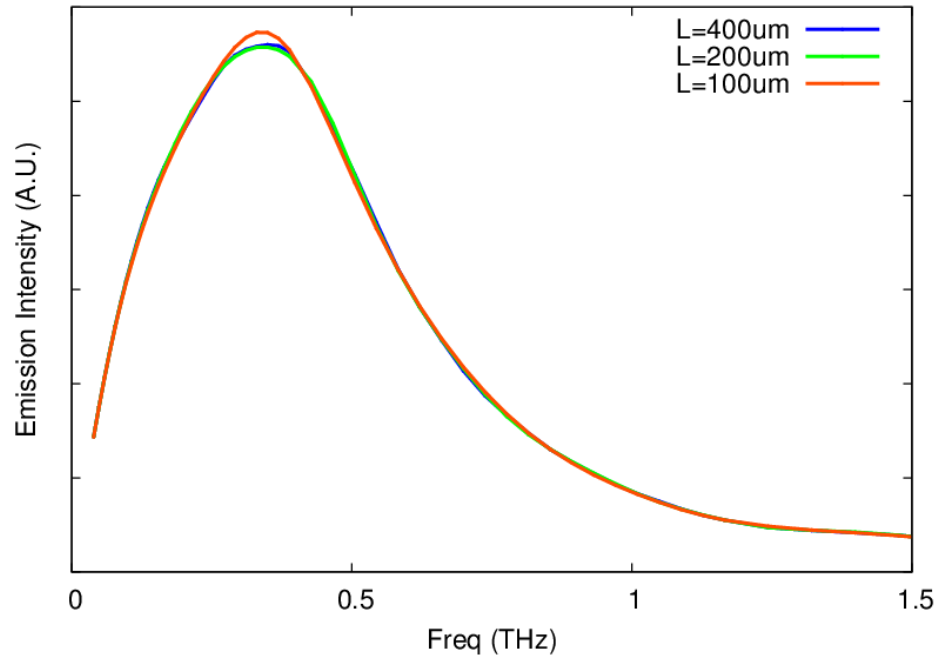
Figure 3.6 - Coplanar Line Length Comparison

The length of the extension of the model volume beyond the antenna structure

perpendicular to the dipole and beyond the long edges of the coplanar lines is called the

bounding box. It is set to an extension length of $b = 50\mu m$. This value was determined

by comparing several lengths between $25\mu m$ and $100\mu m$ as shown in Figure 3.7.
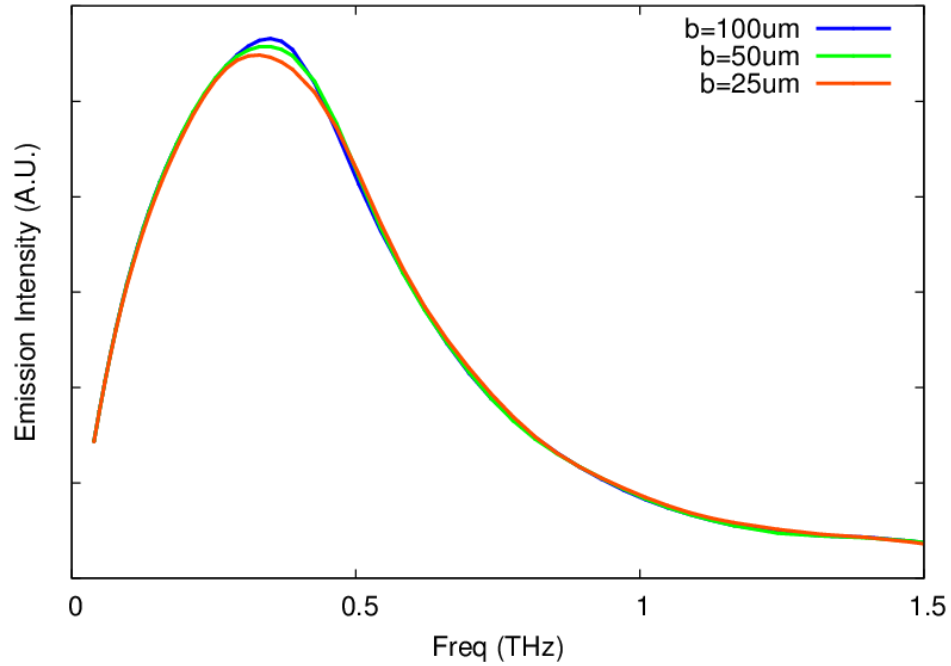
Figure 3.7 - Bounding Box Size Analysis

Although the results of the $50\mu m$ simulation visibly vary from the $100\mu m$ case, it is determined to be a suitable compromise of error and computational time. This bounding box is terminated with an Absorbing Boundary Condition (ABC) boundary. It is determined that this is sufficient by comparing the simulation results with a 4 cell and 8 cell Perfectly Matched Layer (PML) in Figure 3.8.

26
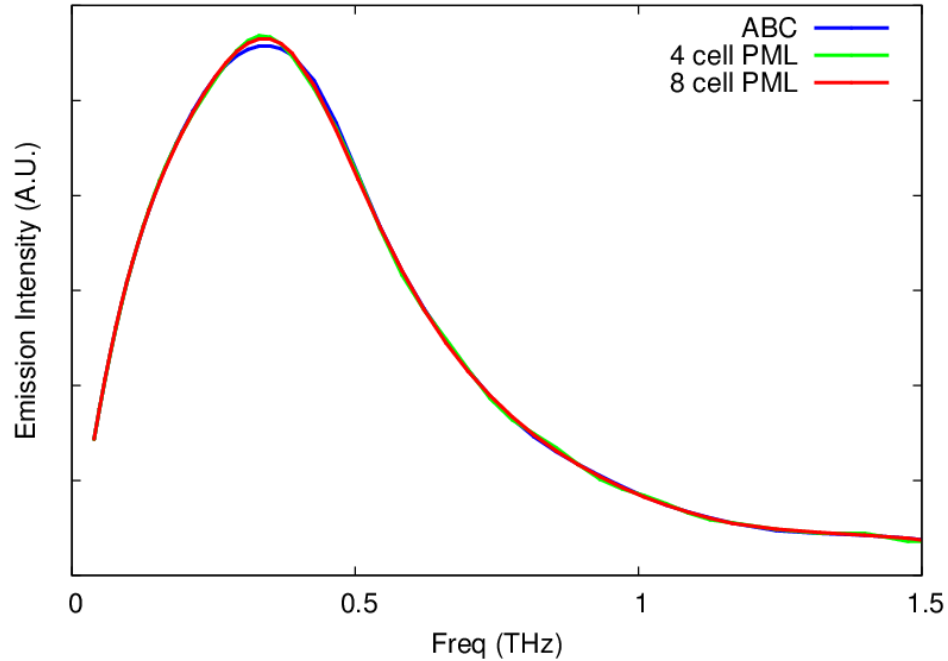
Figure 3.8 - ABC vs. PML Analysis

Using these baseline parameters, additional antenna designs are analyzed and fabricated for further experimental testing and validation.

3.2   Double Sided Dipole

Consider in more detail the double sided dipole. It is expected that modifying the geometry of the dipole including the dipole length and position of the coplanar lines along the dipole will alter the resonant frequency, peak intensity, and bandwidth. In this work, the double sided dipole is defined as a dipole structure with coplanar lines extending away from the dipole in both directions as illustrated Figure 3.9.

27
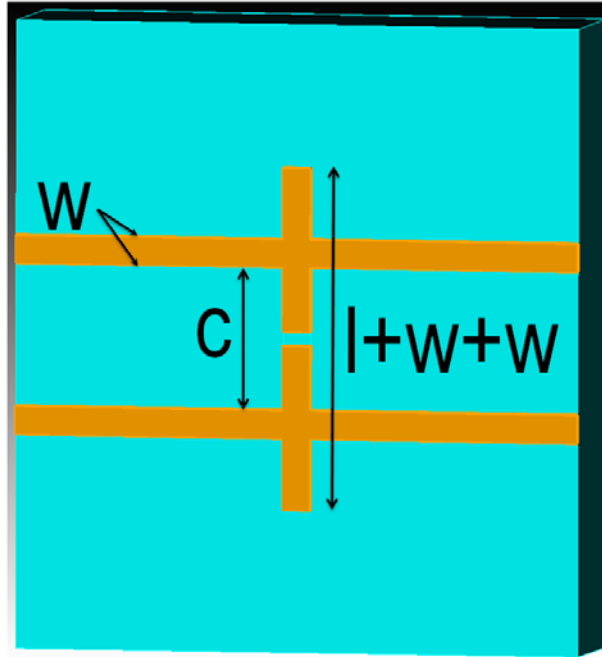
Figure 3.9 - Double Sided Dipole Parameters

Varying the separation between the coplanar lines while keeping the dipole length fixed results in interesting changes in the bandwidth and resonant frequency as illustrated in Figure 3.10.
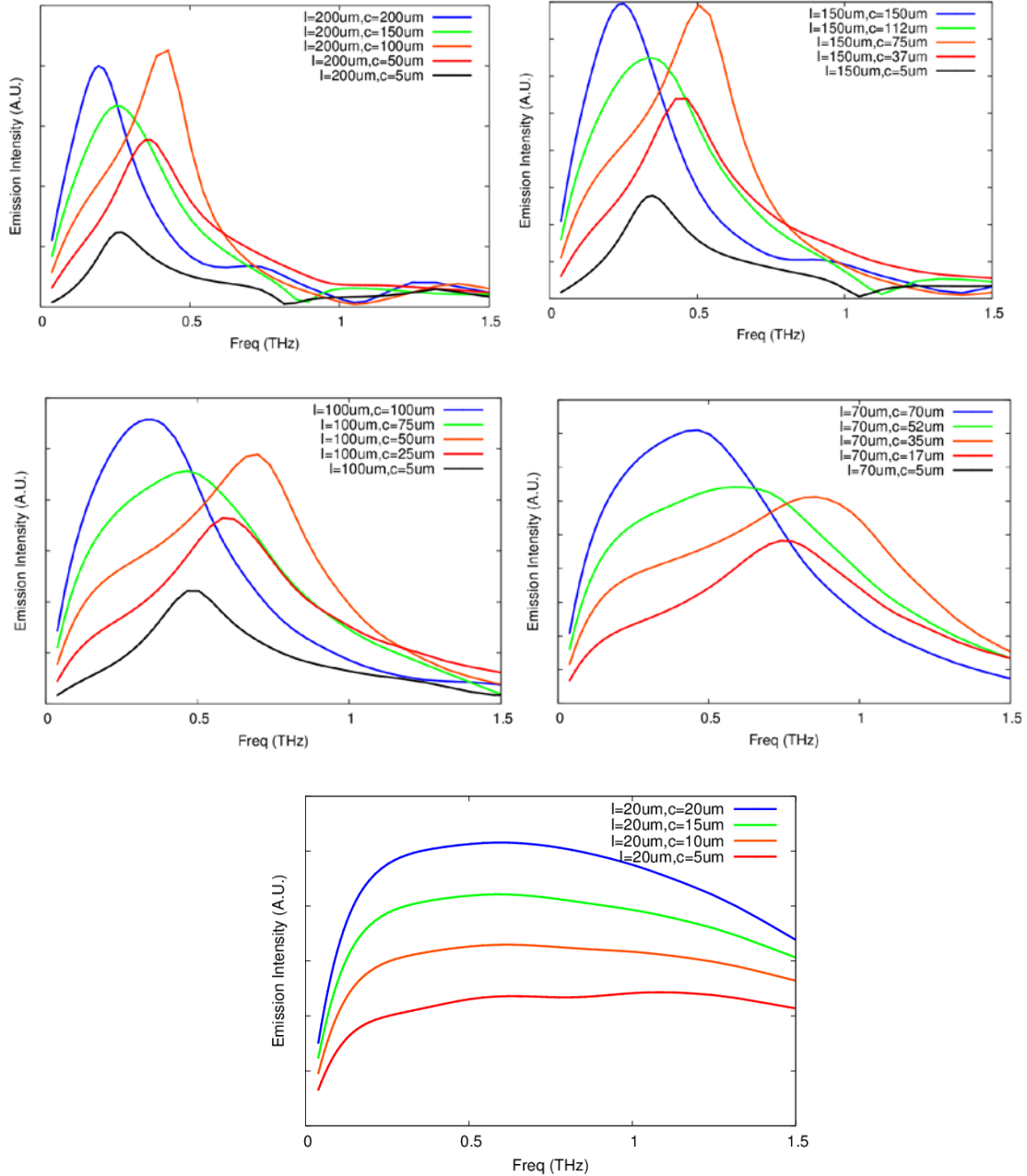
Figure 3.10 – Double Sided Dipole Computational Analysis

It is interesting that in each case except the $20\,\mu m$ case, coplanar lines positioned in the

middle of the dipole seem to resonate another high intensity frequency. This

phenomenon is illustrated more clearly in Figure 3.11.
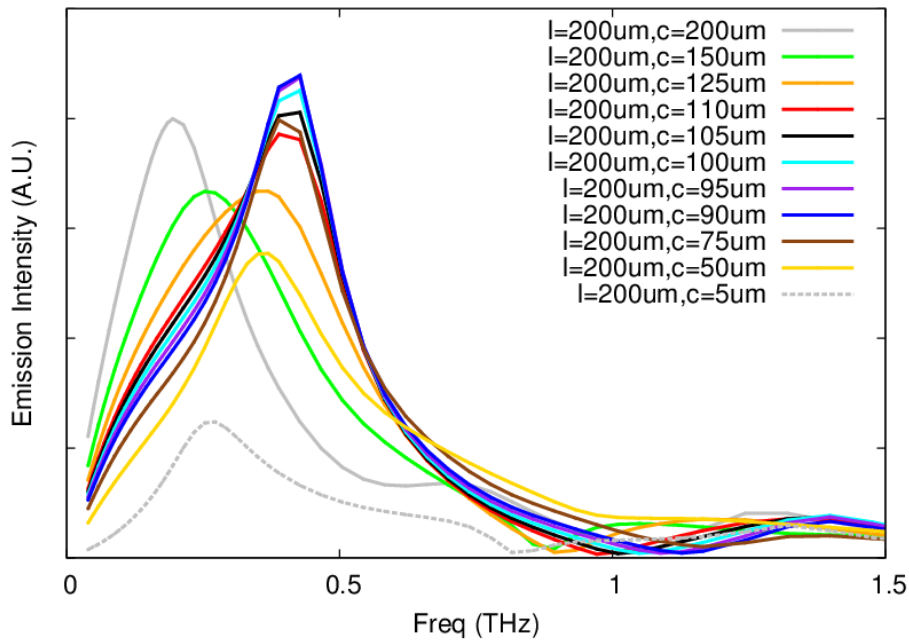
Figure 3.11 - Double Sided Dipole Middle Coplanar Line Resonance

This resonance peaks at a coplanar line separation of $90\mu m$. At this separation, the coplanar lines start $45\mu m$ from the dipole center in each direction meaning they are centered at $50\mu m$ or the center of the dipole length excluding the width of the coplanar line itself. This resonance resembles the effects of a half wavelength dipole in that shortening the coplanar line separation in half results in a near doubling of the resonant frequency. To further verify these results, a subset of double sided dipole antenna is to be fabricated and tested. The parameters of the fabricated antennas are listed in Table 3.2.

Table 3.2 – Fabrication Double Sided Dipole Parameter List

l (in μm)	c (in μm)
20	20
100	100
100	50
100	5
200	200
200	100
200	5

3.3   Single Sided Dipole

The single sided dipole is defined as a dipole antenna with coplanar lines extending away from the antenna in only one direction as illustrated in Figure 3.12. Again, it is not required that the coplanar lines be separated by the full length of the dipole.
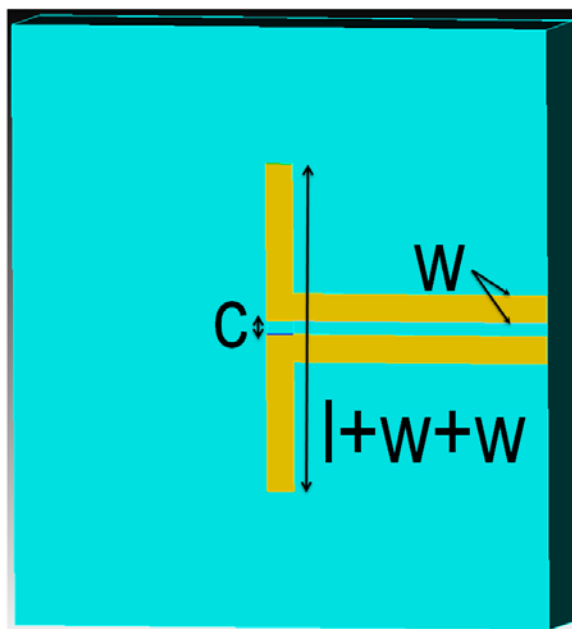
Figure 3.12 - Single Sided Dipole Parameters

A variety of single sided dipole antennas are simulated to illustrate the effects of varying
the parameters on the emission intensity frequency response. A sample of these
simulation results are presented in Figure 3.13.
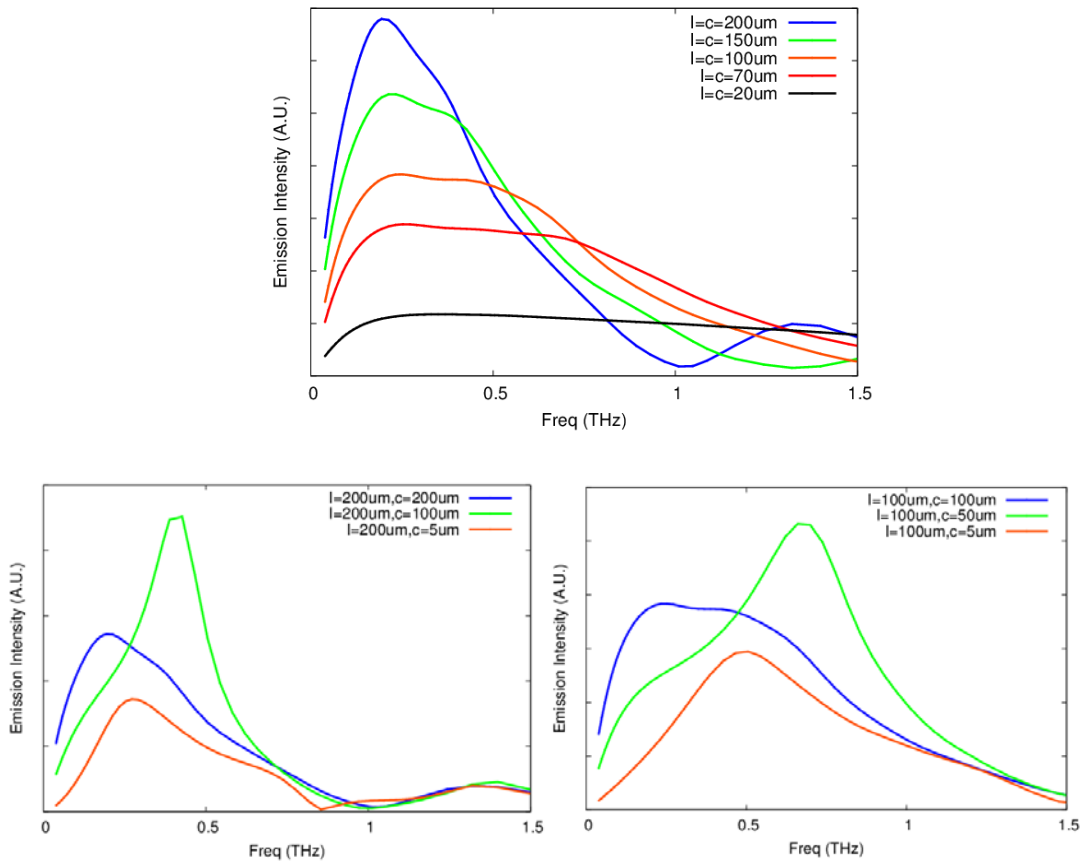
Figure 3.13 - Single Sided Dipole Computational Analysis

Like the double sided dipole, a second resonant frequency is discovered when the
coplanar lines separation is half the distance of the dipole length. Here the peak intensity
of this resonant frequency is much larger than the full separation case. To verify these
results, a subset of single sided dipole antenna is to be fabricated and tested. The
parameters of the fabricated antennas are listed in Table 3.3.

Table 3.3 – Fabrication Single Sided Dipole Parameter List

l (in μm)	c (in μm)
100	100
100	50
100	5
200	200
200	100
200	5

3.4 Bowtie

The bowtie dipole is defined as a dipole structure where the two dipole strips are equivalent trapezoids with the smaller bases meeting at the dipole gap as illustrated in Figure 3.14. In this work, only double sided bowties are considered. This means the coplanar lines extend away from the bowtie dipole in both directions. Again, it is not necessary that the coplanar lines be placed at the larger base edge of the bowties. Instead the separation can be varied to manipulate performance.
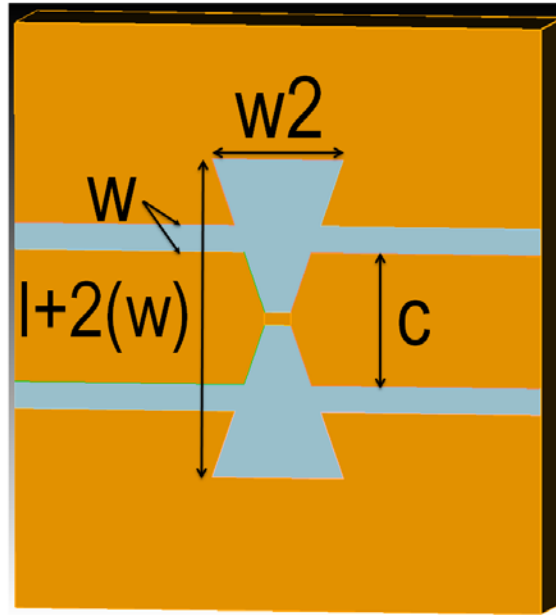
Figure 3.14 - Bowtie Parameters

First consider the effect of the bowtie flare angle or the angle of the trapezoid legs. The most interesting results of the computational analysis are illustrated in Figure 3.15 with the double sided dipole analysis included for reference.
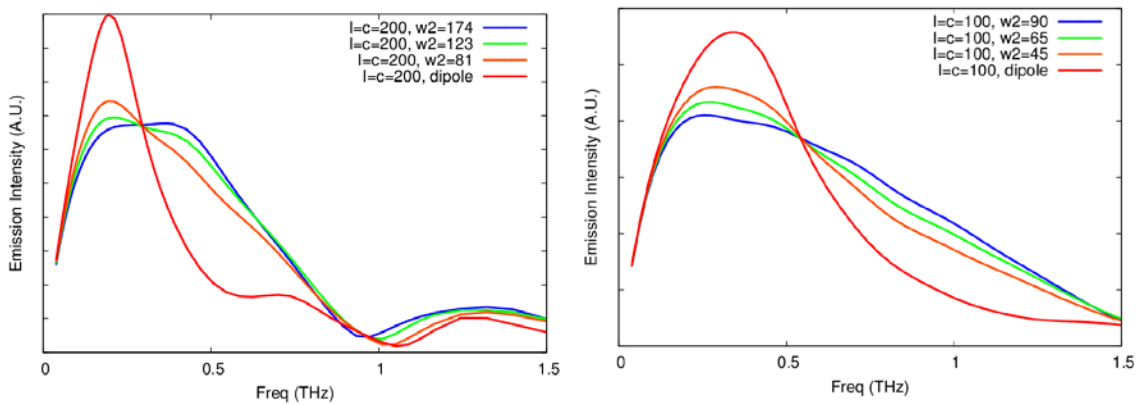
Figure 3.15 - Bowtie Flare Angle Computational Analysis

The results show that as the size of the larger base increases, the frequency response is flattened giving a larger bandwidth at which the intensity is relatively more common. It

is also interesting that each dipole length has a particular frequency/peak intensity point in common with all the flare angles.

Next, consider the separation of the coplanar lines. The results continue to show a resonant point when the coplanar line separation is half the dipole length in agreement with the findings for the dipole cases above. These results are presented in Figure 3.16.
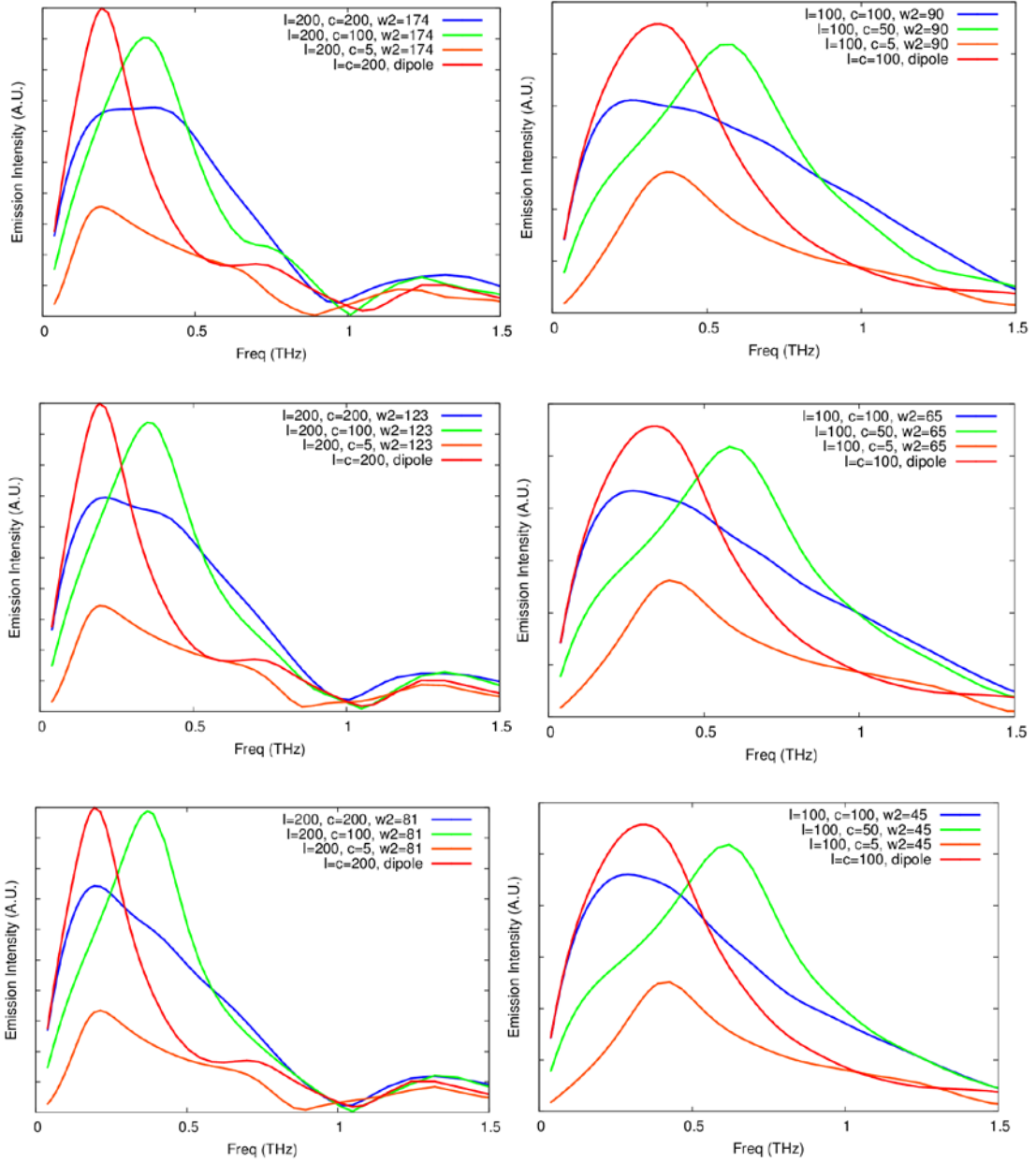
Figure 3.16 - Bowtie Coplanar Line Separation Computational Analysis

To verify these results, the antenna structures described in Table 3.4 are to be fabricated.

Table 3.4 - Fabricated Bowtie Parameter List

l (in μm)	c (in μm)	w2 (in μm)
100	100	27
100	100	45
100	50	45
100	5	45
100	100	65
100	50	65
100	5	65
100	100	90
100	50	90
100	5	90
200	200	44
200	100	44
200	5	44
200	200	81
200	100	81
200	5	81
200	200	123
200	100	123
200	5	123
200	200	174
200	100	174
200	5	174
20	20	13
20	20	15
20	20	19
20	20	23

Several of these antennas have been fabricated by working with Takehito Suzuki at the

Suzuki Laboratory at Ibaraki University in Japan [26]. The antenna structures were

tested using wafers with a low temperature grown GaAs (LT-GaAs) layer and a simple

semi-insulating GaAs layer (SI-GaAs). The LT-GaAs substrate has a much lower carrier

lifetime than the SI-GaAs. The computational analysis is conducted with a carrier

lifetime of 0.5 ps modelling the LT-GaAs. Computational analysis modelling the SI-

GaAs will need to be conducted in the future. The parameters of the antennas

successfully fabricated are listed in Table 3.5. The measurements taken are presented in

Figure 3.17 and Figure 3.18 with the LT-GaAs computational analyses.

Table 3.5 - Successfully Fabricated Bowtie Antenna List [26]

l (in μm)	c (in μm)	w2 (in μm)
100	100	45
100	100	90
100	50	45
100	50	90
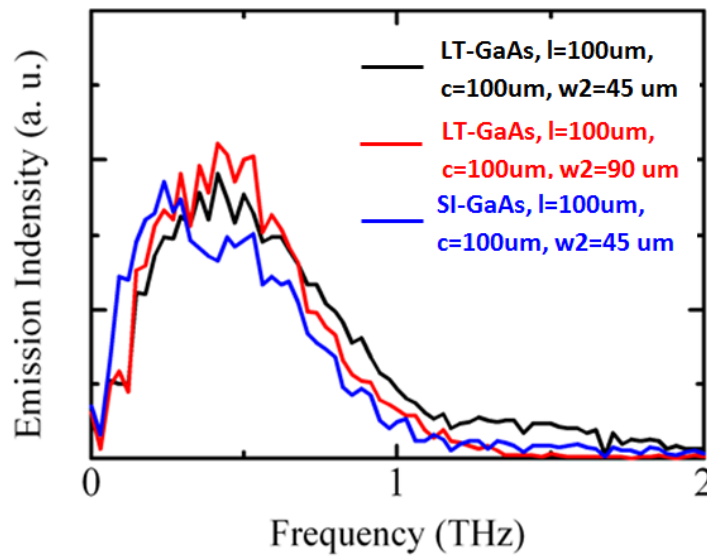
Figure 3.17 - Fabricated Full Coplanar Line Separation Bowtie Antenna
Measurements[26]
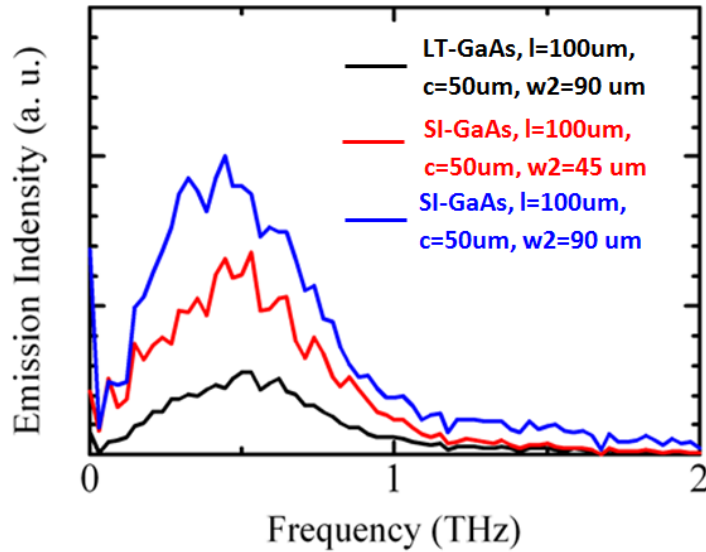
Figure 3.18 - Fabricated Half Coplanar Line Separation Bowtie Antenna
Measurements[26]

Unfortunately the noise level of the measurements is very significant. To minimize the

noise for better comparison, the raw time data is gated off or set to zero after the time

period of interest. The Fourier transform is then performed on the new gated off data.

This removes the late time noise. For example, consider the LT-GaAs full coplanar line

separation bowtie dipole with $w2 = 45\mu m$ (black line) in Figure 3.17. Gating off the

measurements after 10 ps, 15 ps, and 20 ps significantly reduces the noise as illustrated in

Figure 3.19.
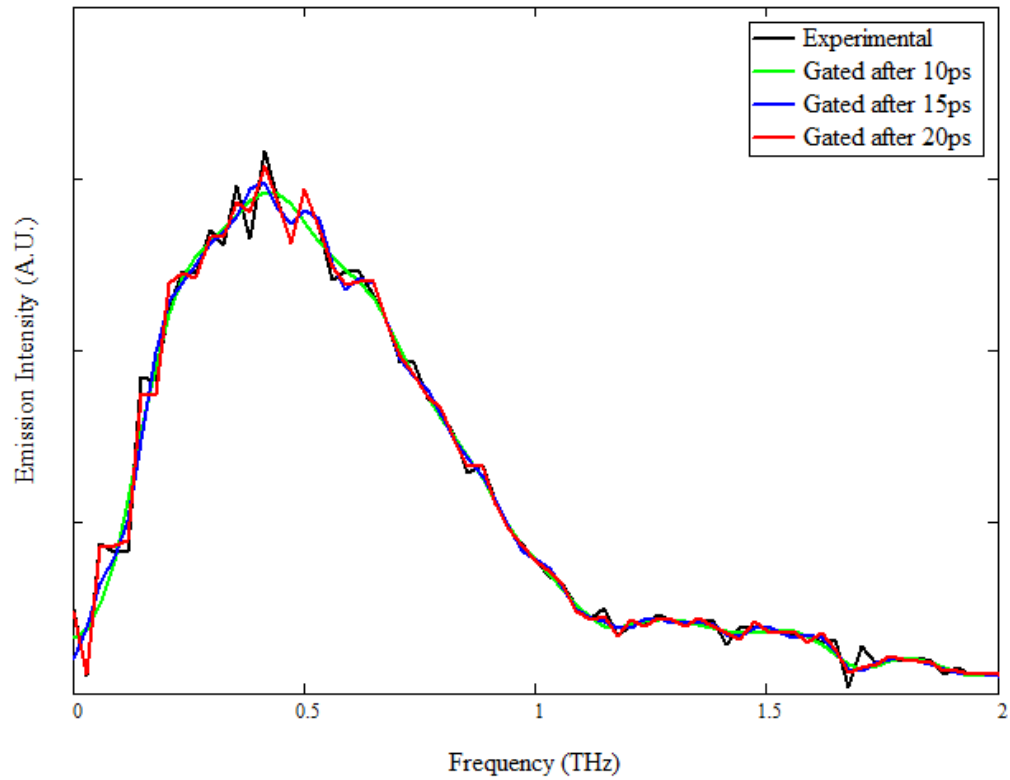
Figure 3.19 - Bowtie Measured Data Noise Reduction Example

Gating off the first 15 ps, measured data is compared with computational analysis in Figure 3.20 and Figure 3.21. The computed results are equally scaled for ease of comparison.
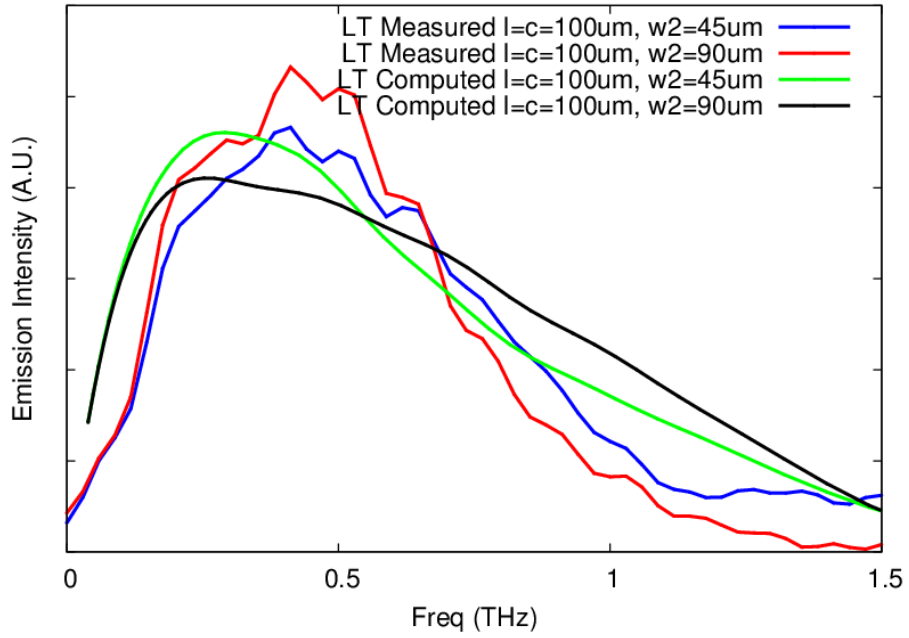
Figure 3.20 - Full Coplanar Separation Bowtie Measured vs. Computed
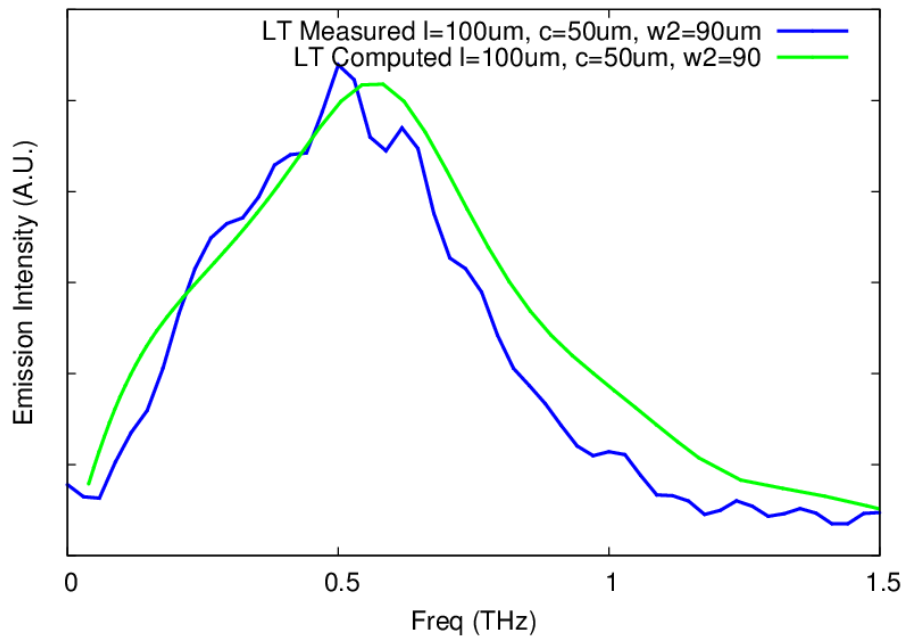
Figure 3.21 - Half Coplanar Line Separation Bowtie Measured vs. Computed

It is noted that both the measured and computed results demonstrate a narrower or sharper peak in the case where the coplanar lines are separated by half the dipole length. This is consistent with the findings for the other structures studied thus far. Otherwise, the results do not match very well especially in the full coplanar line separation case. With such a high level of noise in the measured data, it is possible the measurement is not very accurate even after the gating of late time values. As seen in Figure 5.13 and Figure 5.14, the printing technique used to fabricate these antennas is also not very high quality. Additional testing is needed to determine which result set is most accurate.

3.5   Split-Ring Resonator

Next, structured metal trace geometries are analyzed. Takano, et. al. [27] present metamaterial structures composed of planar metallic resonators called split-ring resonators. Metamaterials are artificially structured materials that can improve the flexibility of electromagnetic systems [27, 28]. Takano, et al. [27] adapt the metamaterial properties of circular split ring structures as presented by Pendry [29] and Smith [30] to form an additional trace ring outside the typical dipole structure coplanar lines. A closed-ring resonator and two split-ring resonators are presented [27] as in Figure 3.22, Figure 3.23, and Figure 3.24.
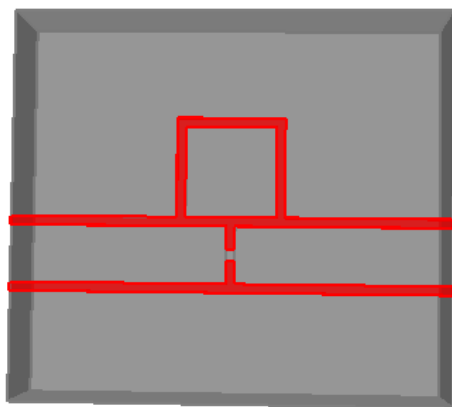
Figure 3.22 - Dipole Circular Ring Resonator (D-CRR)
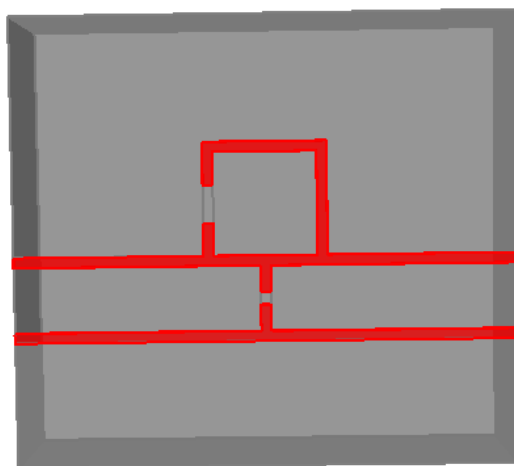
Figure 3.23 - Dipole Split Ring Resonator 1 (D-SRR1)
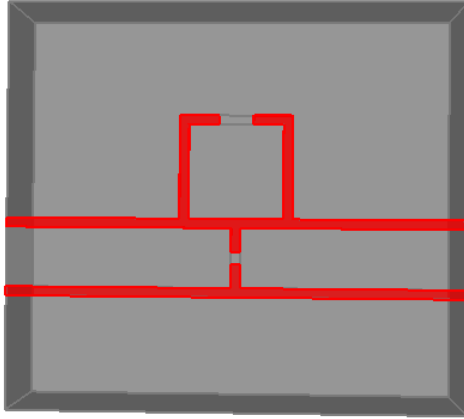
Figure 3.24 - Dipole Split Ring Resonator 2 (D-SRR2)

The split-ring resonator metal rings with gaps determine the total inductance and capacitance of the structure [27]. Therefore, manipulating the parameters of these structures effects the radiation spectra and the radiation efficiency at certain frequencies [27].

Takano, et. al. [27] presents these three structures where the width of the traces is $4\mu m$, the dipole gap width is $5\mu m$, the dipole length is $30\mu m$ from the centers of the coplanar line traces, the square rings are $45\mu m \times 45\mu m$ from the center of the traces, and the split ring resonator gap length is $15\mu m$ where applicable. The structures are fabricated with a superfine ink-jet printer to place silver nanopaste on semi-insulating gallium arsenide (SI-GaAs). The radiation from the antennas is characterized using a spectroscopy system with a Ti:sapphire laser with a 100 fs pulse width, 800 nm center wavelength, and 5.0 mW time average power. A dipole antenna fabricated on low-temperature grown GaAs (LT-GaAs) was used as the detector. Takano, et. al. [27] provides amplitude spectra from experiments and simulations in Figure 3.25. The solid

lines are the x-polarized components and the dotted lines are the y-polarized components.

The spectra are normalized by the peak values of each sample.
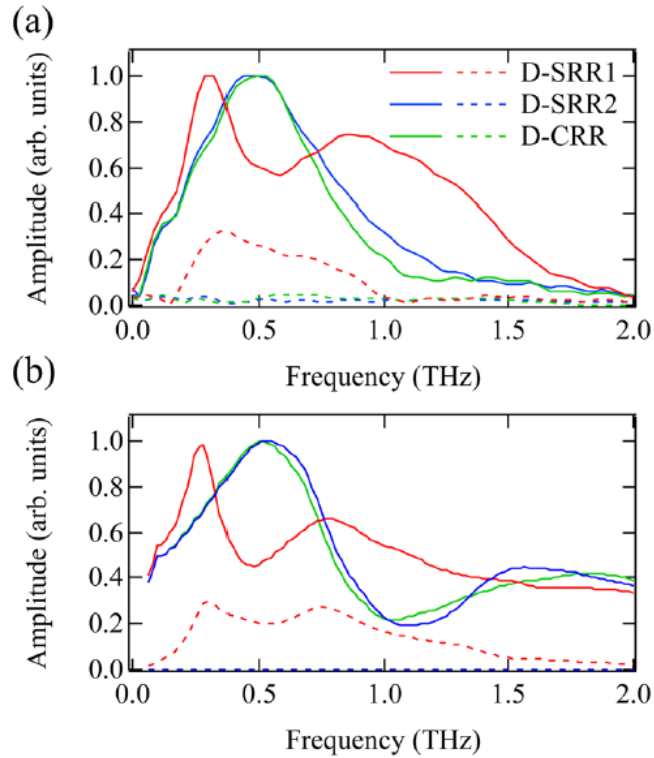
Figure 3.25 - Experimental (a) and Computed (b) Emission Intensities [27]

Computational analysis is conducted using the same free space baseline parameters and wafer characteristics as before with results presented in Figure 3.26.
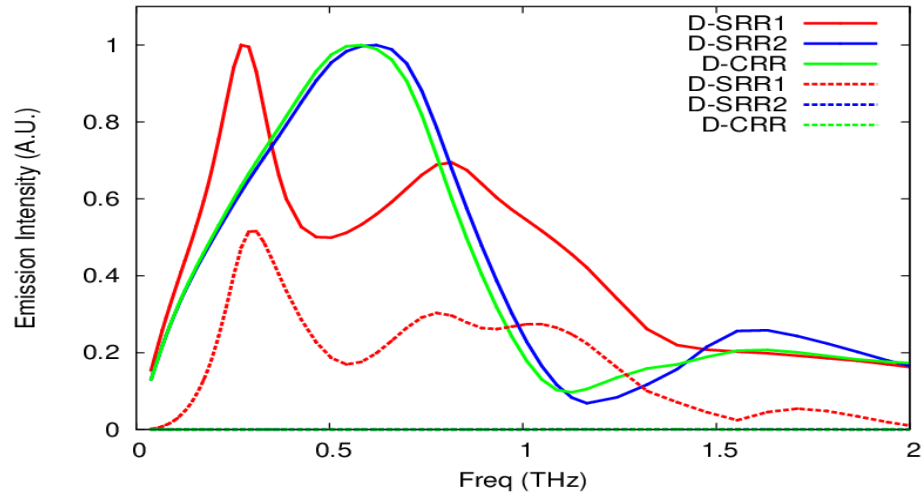
Figure 3.26 - Split Ring Resonator Computed Emission Intensities

These results concur with the findings of Takano, et. al. [27]. It is also interesting that, in this case, a ring with no gap results in very similar results to a ring with a middle gap.

It is intended in the future to fabricate similar structures; however, the trace width presented by Takano, et. al. [27] is so small that trace integrity is expected to be difficult with the currently available photolithography and liftoff procedures presented in Chapter 4. The trace width is therefore increased for the remainder of the models to $10\mu m$ and the other parameters are increased and varied according to the values shown in Figure 3.27. These parameters are varied in order to discover the effects of parameters on the emission intensity frequency response.
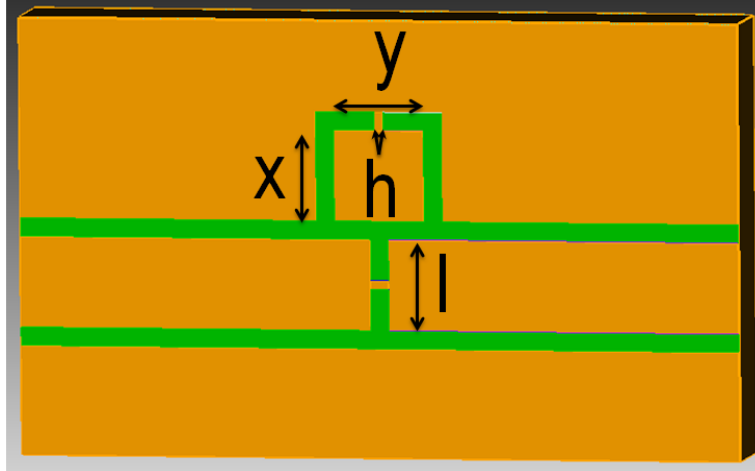
Figure 3.27 - Single Sided Split-Ring Resonator Parameters

Consider the size and location of the gap in the ring. Analysis is conducted

setting $l = x = y = 50\mu m$ and varying the gap size h and the location of the gap from the

side as in Figure 3.23 to the middle as in Figure 3.24. The effects on the frequency

response are presented in Figure 3.28.
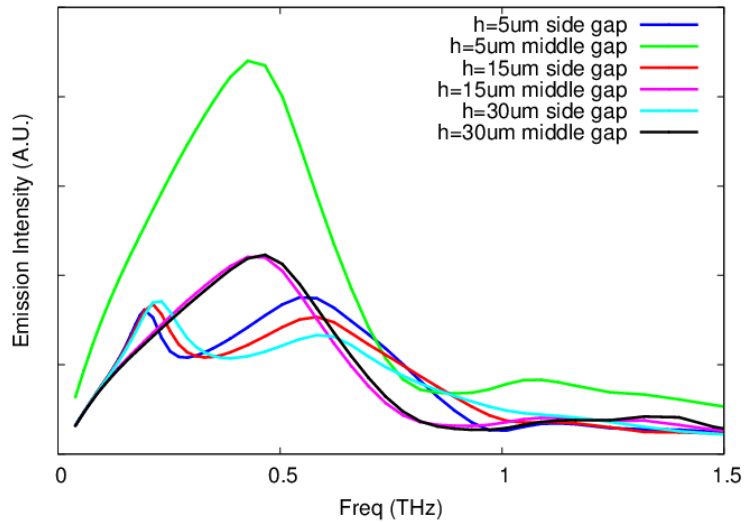
Figure 3.28 - Split Ring Resonator Gap Size and Location Computational Analysis

It is observed that the smaller gaps tend to result in larger emission intensities, especially in the $5\mu m$ middle gap case.

Next, consider the size of the dipole in the structure. Figure 3.29 demonstrates the effects of varying the dipole length l and location of the ring gap while setting $x = y = 50\mu m$ and $h = 5\mu m$.
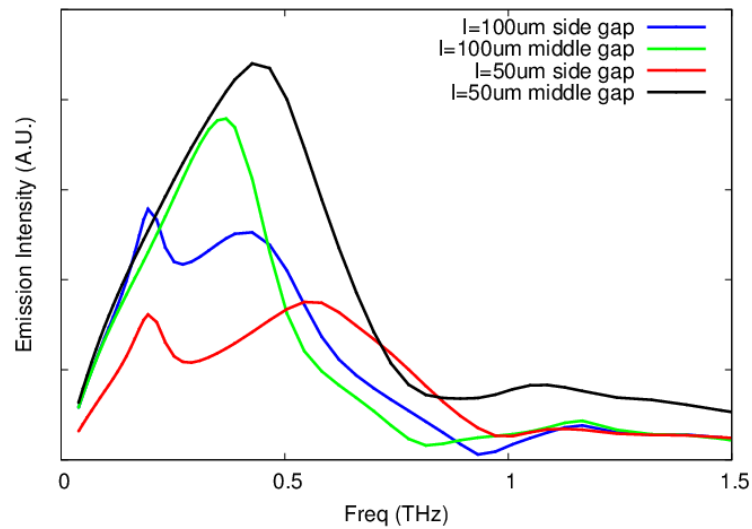
Figure 3.29 - Split Ring Resonator Dipole Length Computational Analysis

It is observed that for the side gap cases, the larger dipole length results in higher peak emission intensity. However, the opposite is true for the middle gap cases.

Consider next the size of the ring. By setting the dipole length $l = 50\mu m$ and varying the x, y parameters and location of the gap, the results in Figure 3.30 can be produced.
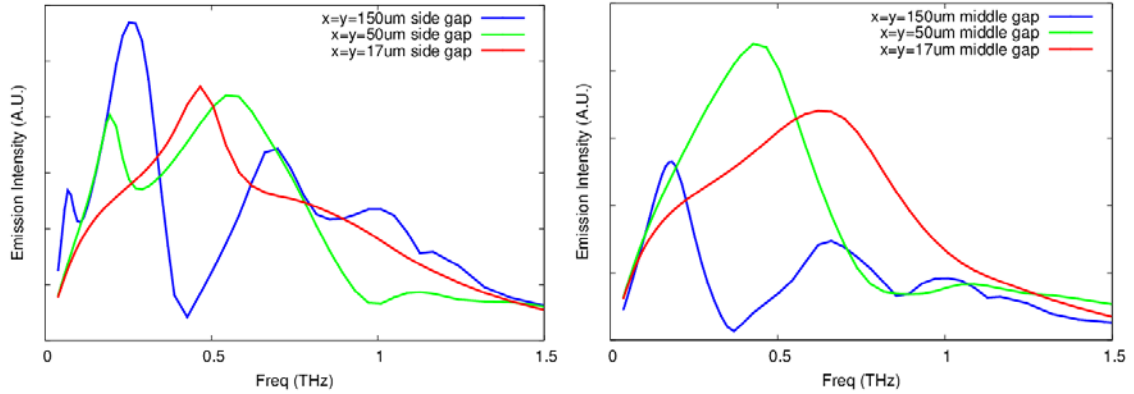
Figure 3.30 - Split Ring Resonator Ring Size and Gap Location Computational Analysis

It is interesting that when the ring is three times the dipole length, the middle gap case begins to imitate the side gap case with multiple peaks. Likewise, when the ring is 1/3 the size of the dipole length, the side gap case begins to imitate the middle gap case with a single resonant frequency.

Finally, consider the position of the ring. The ring can be moved away from the dipole center as shown in Figure 3.31 where o is the horizontal distance from the center of the ring to the center of the dipole.
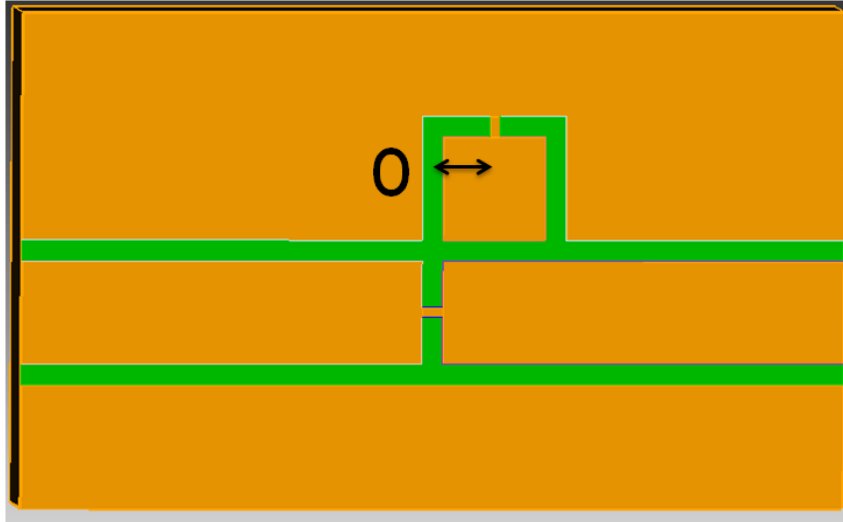
Figure 3.31 - Split Ring Resonator Ring Placement Parameter

When dipole length $l = 50\mu m$, the ring size $x = y = 50\mu m$, and the ring gap $h = 5\mu m$, the position o can be varied such that the frequency response in Figure 3.32 can be generated.
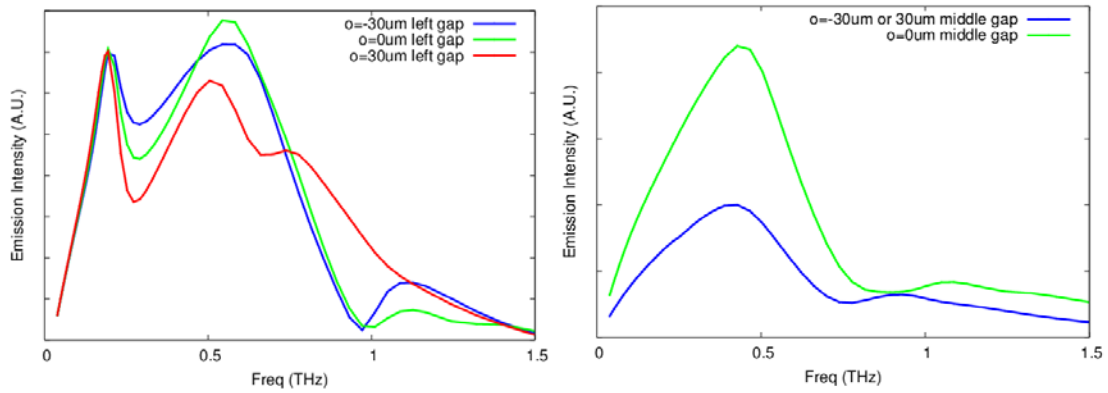
Figure 3.32 - Split Ring Resonator Ring Location Computational Analysis

It is noted that in each case, sliding the ring along the coplanar line minimizes the peak emission intensity with no clear advantages.

3.6 Double Split-Ring Resonator

Further exploration of the effects of these ring structures is investigated by modelling and simulating double ring resonator structures with varying parameters. The additional ring is added on the opposite side of the dipole as the single ring as in Figure 3.33.
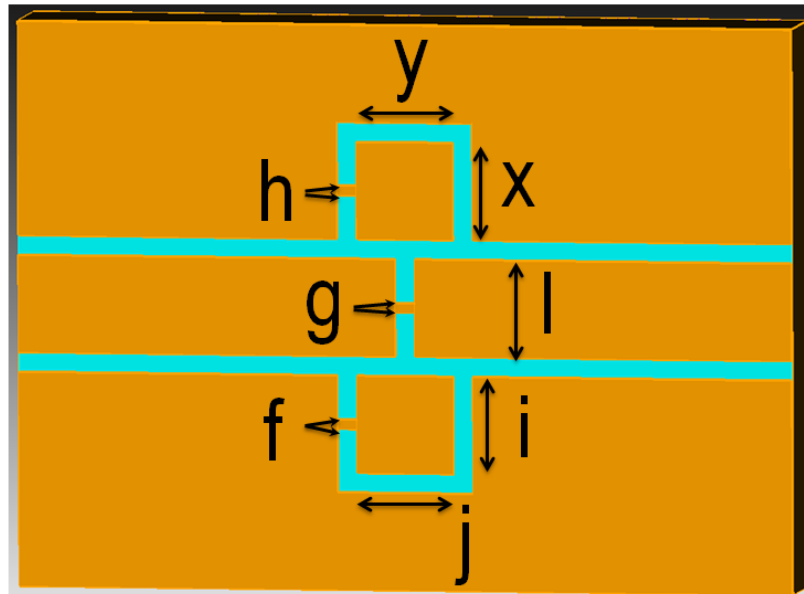
Figure 3.33 - Double Split-Ring Resonator Parameters

Analysis is conducted varying these parameters in order to determine the effects on the radiation spectra and radiation efficiency. These effects are noticed in the following figures which include the reference single split ring resonator and various ring gap placement. Figure 3.34 presents the effects of having all the gaps on the side of the rings. Figure 3.35 presents the effects of mixed gap locations on the two rings. Figure 3.36

presents the effects of having all the gaps in the middle of the rings. The gap lengths are

set as $h = g = f = 5\mu m$ and the dipole length is set as $l = 50\mu m$.
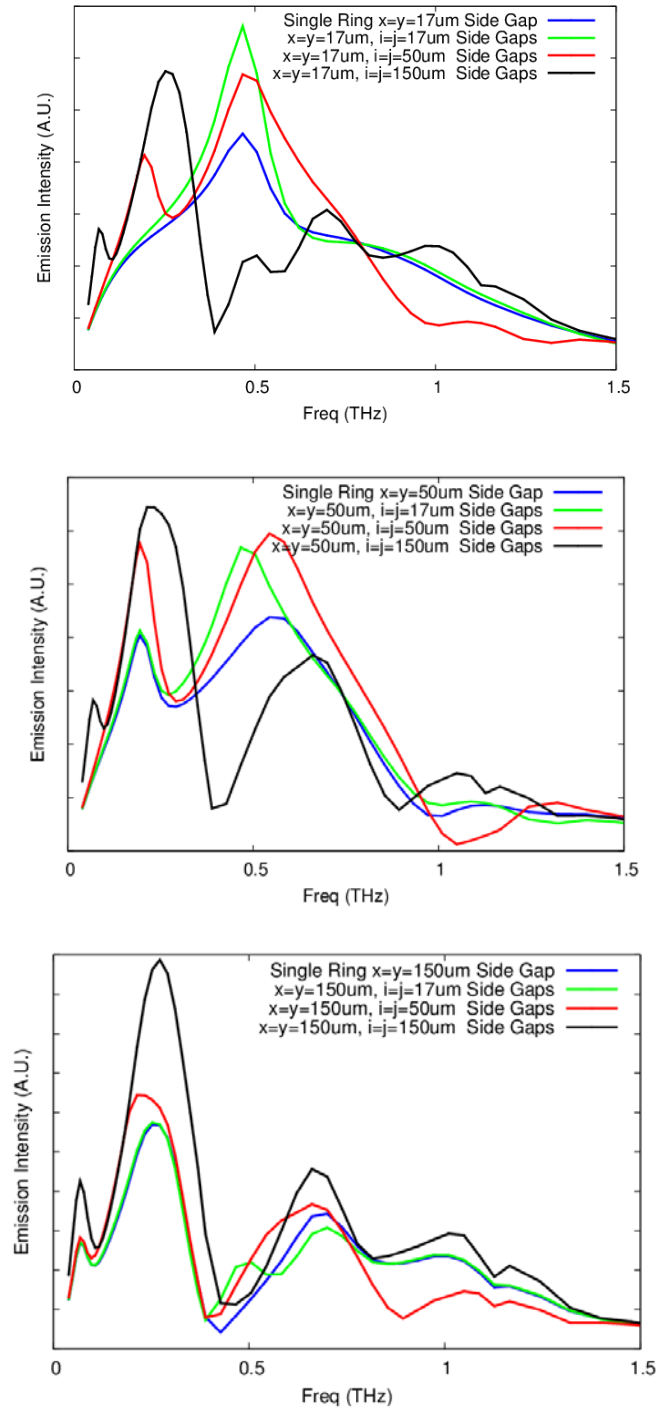
Figure 3.34 - Double Split Ring Resonator Side Gaps Computational Analysis
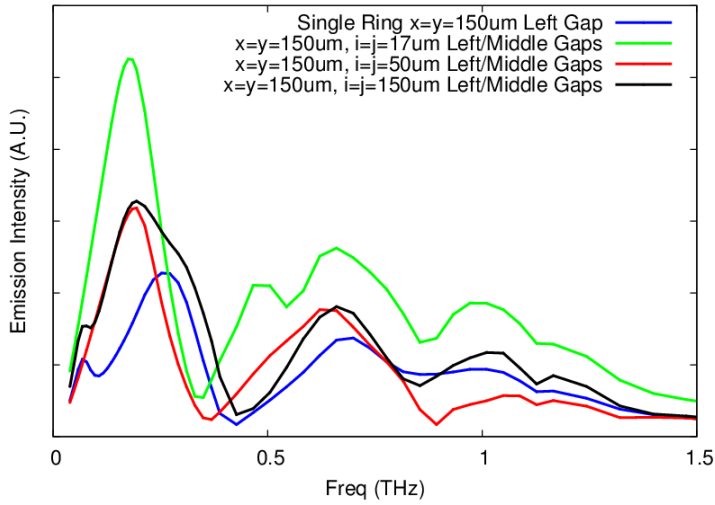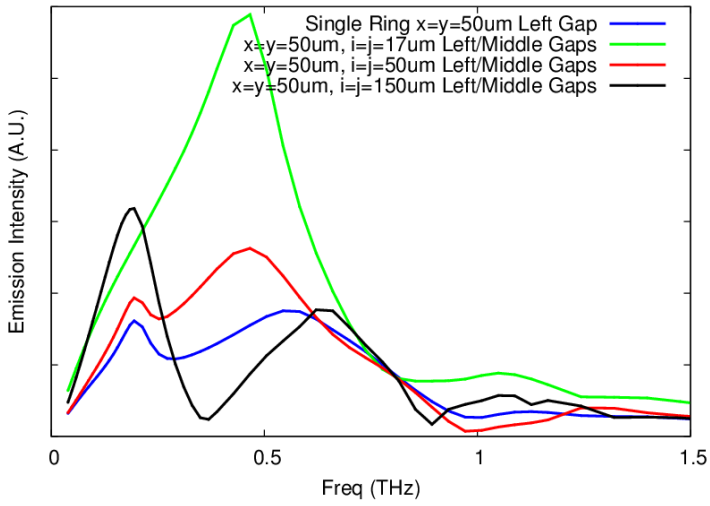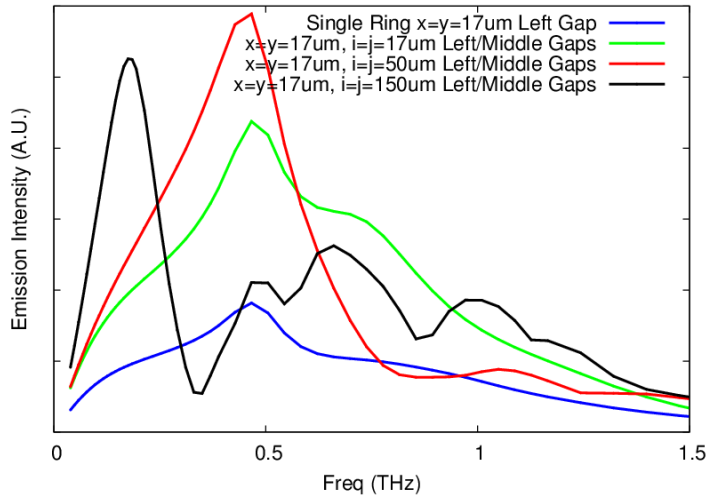
Figure 3.35 - Double Split Ring Resonator Left/Middle Gaps Computational Analysis
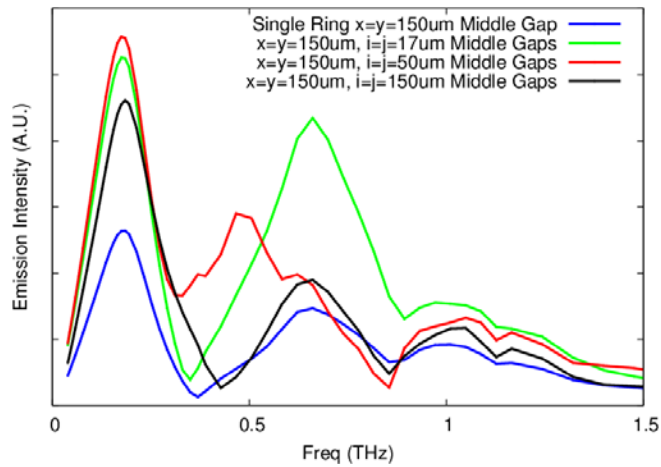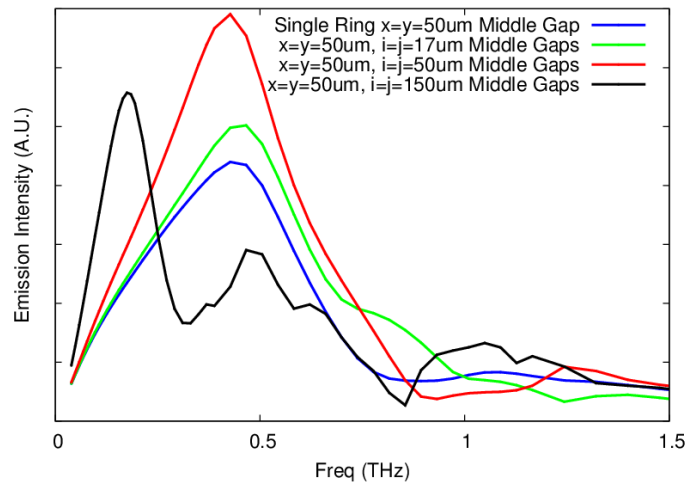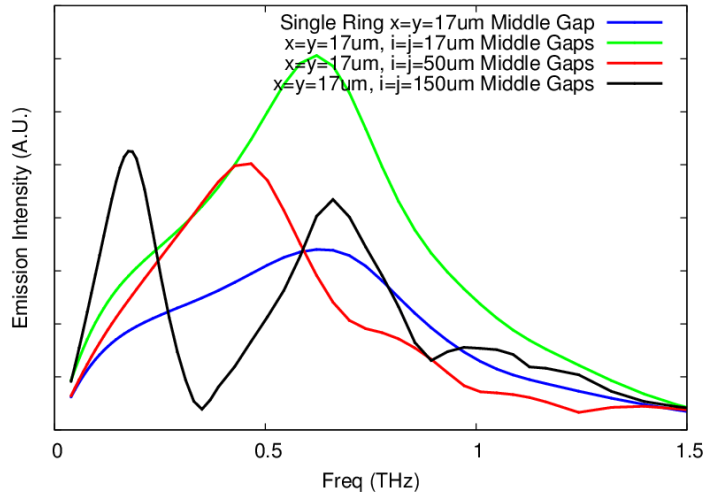
Figure 3.36 - Double Split Ring Resonator Middle Gaps Computational Analysis

It is observed that the additional ring increases the peak intensities. This effect is most

pronounced in the cases where one ring has a side gap and the other has a middle gap.

3.7   Bowtie Split-Ring Resonator

Finally, the bowtie dipole structure is combined with the split-ring resonator to create

Bowtie Split-Ring Resonator structures such as in Figure 3.37 and Figure 3.38.
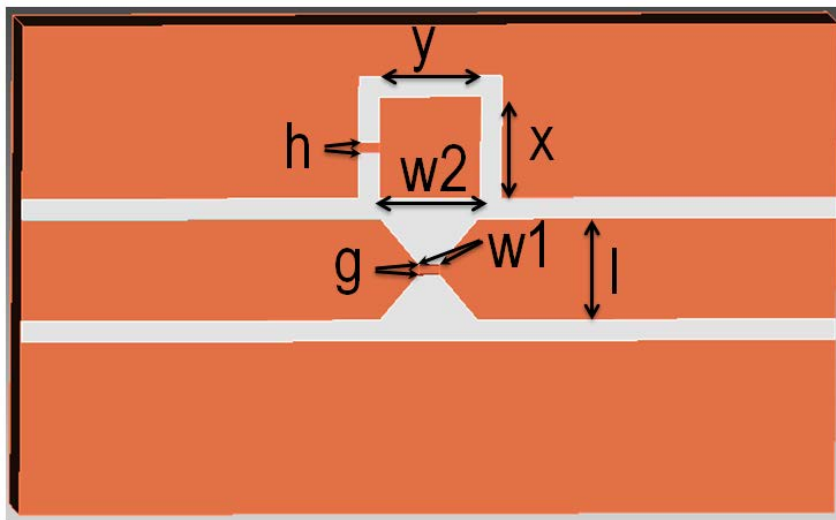
Figure 3.37 - Single Split-Ring Resonator Bowtie Parameters
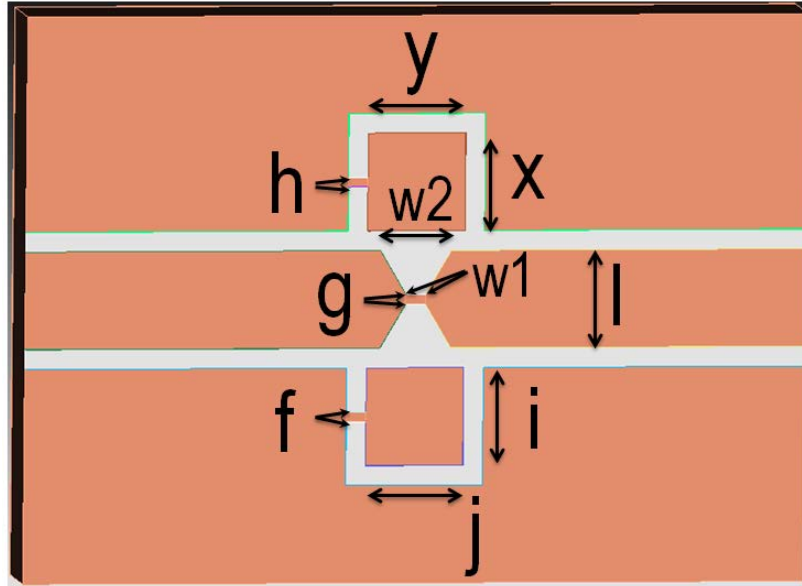
Figure 3.38 - Double Split-Ring Resonator Bowtie Parameters

Computational analysis is again conducted with the same free space baseline parameters as before to determine the effects of varying some of the bowtie parameters and the position of the ring gaps with the results presented in Figure 3.39, Figure 3.40, Figure 3.41, and Figure 3.42. The baseline parameters are set to a dipole length $l = 50\mu m$, ring sizes $x = y = 50\mu m$ and $i = j = 50\mu m$ where applicable, gap lengths $g = h = f = 5\mu m$, and bowtie small base length $w1 = 10\mu m$.
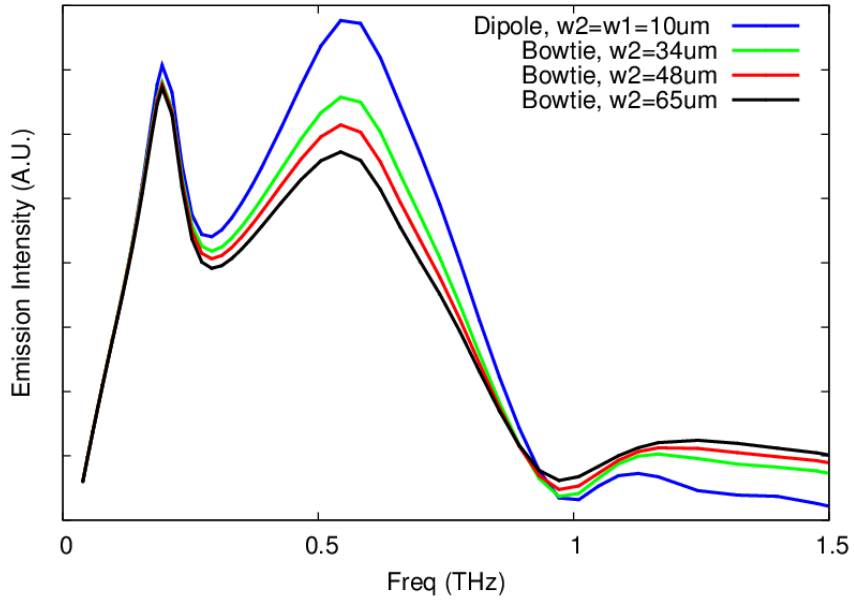
Figure 3.39 - Single Split-Ring Resonator Bowtie with Side Gap Analysis
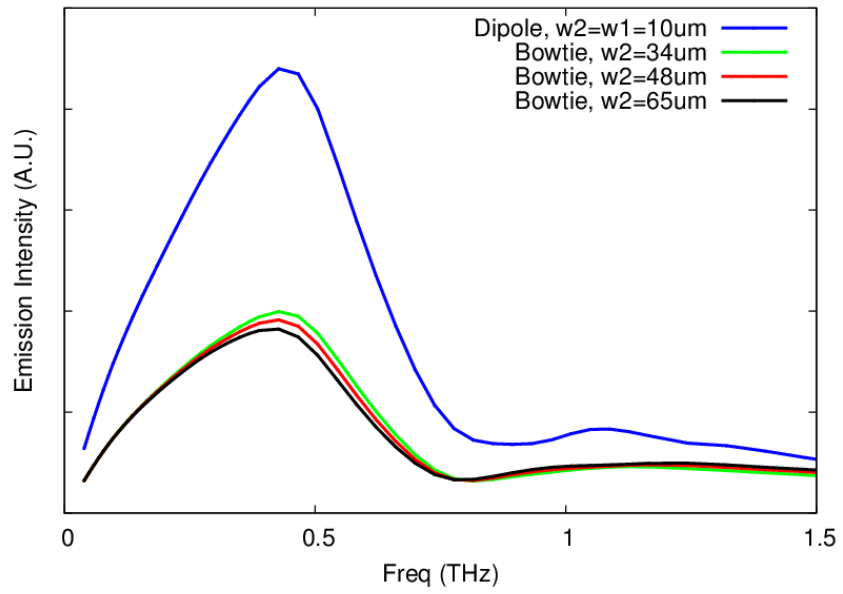
Figure 3.40 - Single Split-Ring Resonator Bowtie with Middle Gap Analysis
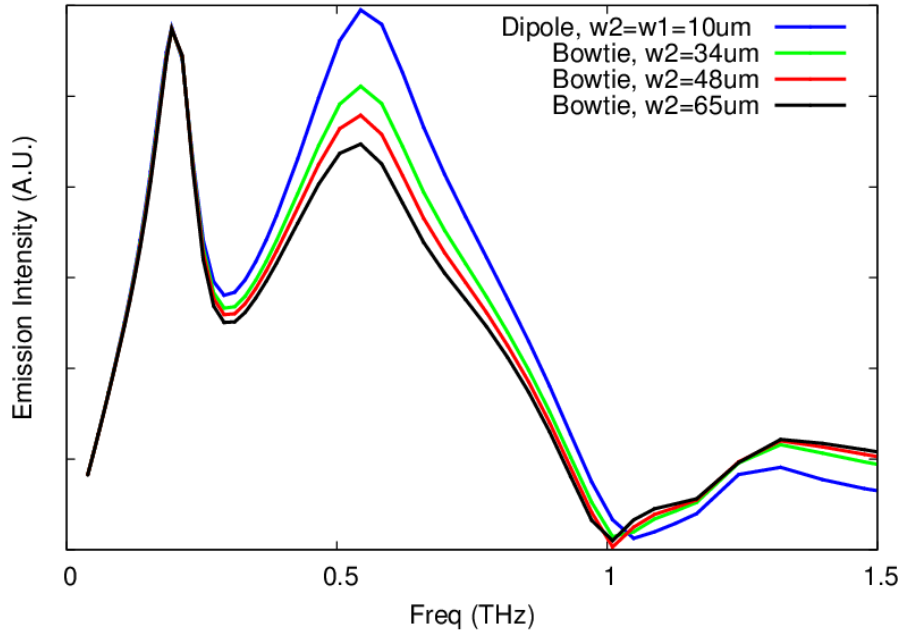
Figure 3.41 - Double Split-Ring Resonator Bowtie with Side Gaps Analysis
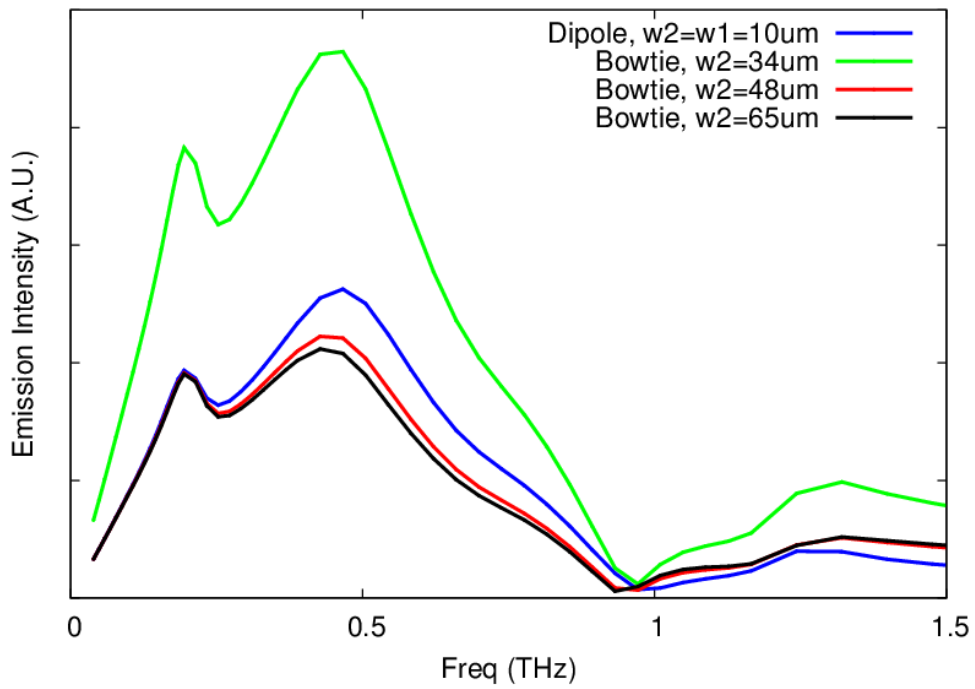
Figure 3.42 - Double Split-Ring Resonator Bowtie with One Side and One Middle Gap Analysis

It is noted that the addition of the bowtie in the single ring cases significantly decreases the peak intensities without adding a noticeable benefit. The double ring structure with both rings having side gaps also follows this behavior. However, it is interesting that the double ring with one side gap and one middle gap shows great improvement in the peak intensity for the smaller flare angle.

3.8   Summary of Results

In summary, the computational analysis method presented in Chapter 2 has been validated using the full double sided dipole antenna. In addition, using double sided dipole, both the mesh and simulation parameters were optimized. The method was also validated for the bowtie, and split-ring resonator structure using published literature and results from testing. The simulated results compared quite well with the measured data. Slight differences in the peak emission intensity for the smaller full double sided dipole are theorized to be due to effects such as conduction losses and additional resistances in the complete spectroscopy system that were not included in the simulation, as well as non-ideal laser spot size. In the case of the bowtie antenna, the measured data is very noisy and variations from the computational analysis are most likely due to the quality of the fabricated structures and the contributions of the detecting antenna.

After gaining confidence in the accuracy of the DGFETD simulation to estimate the emission intensity of photoconductive THz antennas, a study of a variety of antenna geometries was conducted. It was found that reducing the separation of the coplanar lines of the dipole and bowtie antennas in half results in a strong resonant peak in emissions at nearly twice the frequency as compared to a full separation of the coplanar

lines. It was also discovered that the bowtie structures result in a flattened response area at peak emission intensity, providing a broader bandwidth. It is also shown that in the case of the split-ring resonators, the ring size and gap positions vary the resonant frequency in a manner that seems consistent with adjusting the dipole length appropriately. Further study is required to determine the exact correlations. It was also found that the addition of a second ring in the split-ring resonator structure results in greater peak emission intensities.

4 FABRICATION OF DEVICES

4.1 Description of Devices

The multi-physics port model and DGFETD method are validated with the experimental data presented by Miyamaru, et al. [25] and Takano, et al. [27] for the standard dipole and ring resonator structures, respectively. Further validation is conducted with the experimental results of the bowtie antenna conducted with Suzuki. More complete validation is accomplished by fabricating the other antenna designs presented in Section 3.

A common currently used photoconductive substrate is Gallium Arsenide (GaAs) due to its lower cost and higher availability. A layer of low temperature GaAs can be grown on top of the typical GaAs to increase the recombination rate of the carriers. The carriers need to recombine quickly in the detecting antenna. This low temperature grown layer provides a very short carrier lifetime[31] as well as semi-insulating properties[32]. Therefore, the first fabrication attempt was done on a 500-600 µm SI-GaAs substrate with 1-2 µm layer of low temperature GaAs (LT-GaAs) grown on top at a temperature of $200 - 250\ ^o$C. It was annealed for about 10 minutes at $600\ ^o$C after growth. The wafer had a 2 inch (50.8 mm) diameter and [100] crystal orientation. A commercially available antenna was also purchased (see Figure 4.1). Later fabrication attempts were made on polished undoped SI-GaAs 4 inch wafers that were 625 μm thick. These wafers have a resistivity greater than $10^7 \Omega cm$.
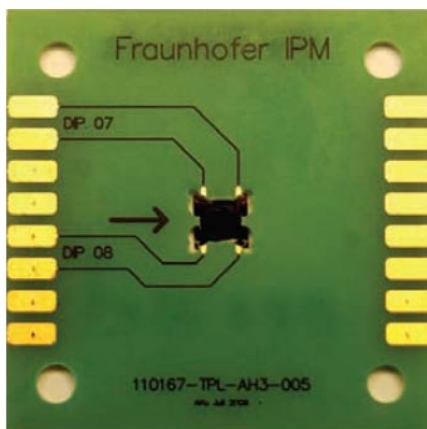
Figure 4.1 - Menlo Systems Tera8-1 THz Antenna

Titanium gold (TiAu) traces were used for the antenna structures due to availability at the time of fabrication and thermal stability. The interface to the antenna is vitally important to the functionality because of the picosecond high voltage switching (such as photoconductive switches). Ohmic contacts with negligible contact resistance are preferred in this case to most accurately represent the computational model and make the best possible connections to external circuitry. Heating of the switch may lead to failure [33] with significant contact resistance. It has been determined that a AuGeNi alloy is far more effective than a straight Ti/Au metal layer [34]; however it was not available at the time. Vieweg, et al. [35] have found that annealed ohmic contacts fabricated using a Ni/AuGe/Ni/Au layer stack with 5/90/25/50 nm thickness and subsequent annealing at 420 ^{o}C for 90 seconds offer about twice the output signal intensity as TiAu metallization. Vieweg [36] has also found that TiAu is more thermally stable and less reactive than AuGe since titanium has a much higher melting temperature than gold or germanium.

The fabrication of these devices was done using the facilities of the Center for Nanoscale Science and Engineering (CeNSE) located at the University of Kentucky. The fabrication process included photolithography, application of the trace metals, liftoff, and cleaving with the necessary cleaning techniques required at each step. After fabrication of the antenna structures, the cleaved wafer sections were then embedded into printed circuit boards so that they can be tested in a spectroscopy system.

4.2   Photolithography

The first step in the fabrication process is photolithography. In photolithography, photoresist is applied to the wafer and then desired patterns are removed leaving bare surface for metal deposit. There are two different photoresist processes, positive and negative. With positive photoresist, the layer of applied photoresist is exposed to UV light in the areas where it is desired that the photoresist be removed leaving the areas for desired metal traces. This occurs because the UV light changes the characteristics of the photoresist so that it is more soluble in the developer. Therefore, after exposure when the wafer with photoresist is subjected to the developer solution, the photoresist exposed is removed. The other method uses negative photoresist. In this process, the areas of photoresist exposed to the UV light become more resistant to the developer such that application of the developer solution removes all areas that were not exposed.

In this particular fabrication, positive photoresist is used therefore an image mask was created that is clear in the areas where metal traces are desired and opaque elsewhere. The first mask created included 2 copies of 42 antenna structures positioned

63

on 6 different blocks separated by dicing "streets" or areas for separating the blocks.

These 42 antenna structures include the full list of double sided dipole, single sided

dipole, coplanar lines only, and bowtie structures presented in Section 3. Each fabricated

antenna has coplanar lines 2 mm long in each direction from the center of the dipole gap

(where applicable) with a $100 \, \mu m$ by $100 \, \mu m$ pad at the outer end for connection to an

external printed circuit board so that connections can be made during testing. The mask

is designed such that ½ of the wafer is utilized thus saving the other half for a later

attempt.
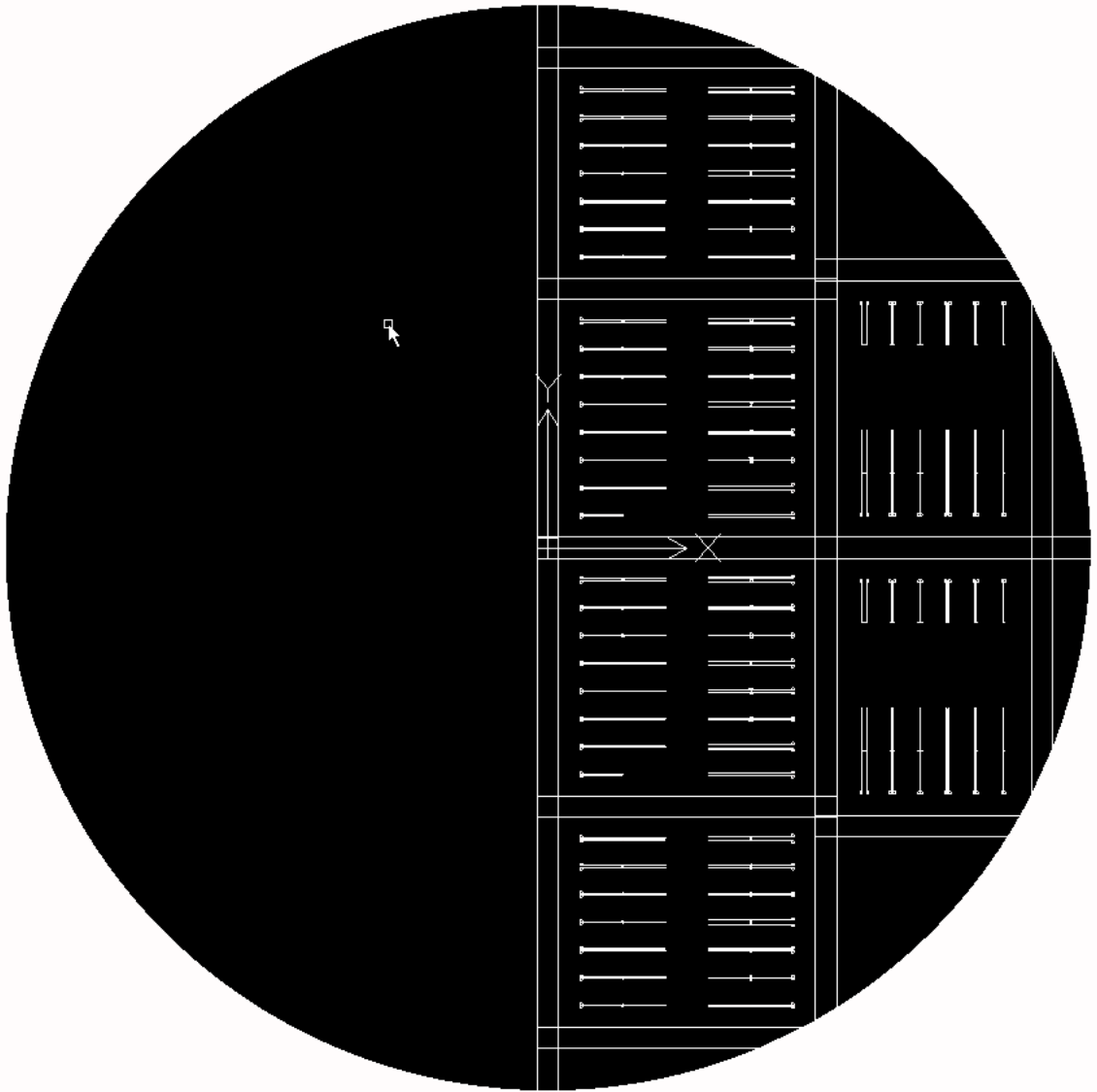
Figure 4.2 - First Exposure Mask

In order to process the wafer and mask such that the photoresist protects the areas

between traces and bare wafer is exposed where traces are desired, the GaAs wafer is first

coated with positive photoresist. In this case, S1813 photoresist from Shipley is used.

According to the documentation provided by Shipley (see

http://nanofab.ece.cmu.edu/resources/s1800seriesDataSheet.pdf), spin coating S1813 at a speed of 2000 rpm provides a layer of photoresist about 19,000 Angstroms (or 1,900 nm) thick. The optimum ratio of photoresist thickness to trace thickness for successful sputtering is approximately 10:1.

After the photoresist is applied, the wafer is placed on a hot plate of 95 $^{\circ}$C for 1 minute so that the photoresist can set properly. After cooling, the coated wafer is then aligned and placed in contact with the mask while ultraviolet (UV) light is illuminated. The mask and wafer are illuminated for 9 seconds to adequately expose the transparent areas of the mask so that all the photoresist is removed during development but not to over expose such that the fine dimensions of the structures are sacrificed.

After exposure, the wafer is placed in a Shipley microposit MF-319 developer solution for at least 1 minute so that the (UV) exposed photoresist is dissolved away. Then the wafer is rinsed in ultra-pure water (H_2O) and dried. Once dry, it is placed under a microscope to verify that the antenna patterns are removed properly for metallization. If the process has gone as desired, the wafer is placed back on a hot plate of 95° C for a few minutes to prevent further undesired changes. In instances where the process needs to be repeated, the photoresist layer is removed by applying acetone followed by isopropyl alcohol (IPA) and then a thorough rinsing and drying. This process is repeated as much as necessary to determine the correct equipment settings and achieve the desired result.

4.3   Application of Metal and Liftoff

Proper wirebonding at the University of Louisville requires a pad thickness of 250 – 300 nm. It is common to use a 20% Ti to 80% Au ratio.[37] Therefore, the traces are applied by applying 50 nm of Ti and then 200 nm of Au. This metallization layer is applied to the entire wafer after photolithography. When properly coated the photoresist is lifted off removing the metal from the areas outside the traces.

In preparation for the metal deposit, the wafer is first cleaned of organic particulates to ensure clean access to the GaAs. This is accomplished using oxygen plasma ashing. Plasma ashing uses partially ionized oxygen to remove organic matter from the wafer. Two common contaminants removed in this matter are carbon oxides and water vapor. It is particularly important to remove these contaminants in the case of applying titanium due to its high susceptibility to oxidation. It is also important to note that oxygen plasma ashing will also remove photoresist so it is critical to limit the amount of ashing at this point so that contaminants are removed but the vast majority of the photoresist remains intact for metallization and liftoff. Therefore, at this point the sample is ashed for only 30 seconds.

The process of oxygen plasma ashing is performed in a modified microwave oven designed for this purpose in CeNSE. This machine is fitted with a vacuum pump, oxygen supply, and vacuum chamber. First, the sample is placed in an air tight chamber consisting of a Pyrex dish over a sealing mat in the oven compartment. The vacuum pump is used to vacate the air from the chamber. Then oxygen is supplied to the chamber at a pressure of about 1 mbar. When the microwave is activated, the oxygen is partially ionized creating a plasma around the sample that bonds with organic materials on the

surface. When finished, the oxygen is turned off and the vacuum pump is again applied to remove the lifted contaminants before restoring normal air pressure and removing the sample. This process is done immediately before metallization to ensure the wafer is as free of contaminating organics as possible.

As for depositing the metals, the first three attempts were all made using sputtering. Sputtering is a process of coating a sample with a thin film from a particular target material. The equipment used in this experiment was a small plasma sputterer in CeNSE. The sample is placed on an anode surface in a vacuum chamber opposite a cathode target composed of the material to be deposited. Process gases are used to create a plasma under vacuum which bombards the target material and ejects molecules onto the sample. It is important that the projectile mass match the target mass for efficient momentum transfer and maximum energy transfer. In this case, the inert gas argon is used. The plasma is created by the collision of high energy electrons (accelerated from the cathode toward the anode) with the neutral atoms. As the current grows, there is eventually enough ions and electrons for the plasma to be self-sustaining. It is important to maintain the proper gas pressure during this process. If the pressure is too low, insufficient collisions will occur due to the lack of atoms. If the pressure is too high, the overabundance of atoms will cause too many collisions and the electrons will not gain sufficient energy to ionize the gas.

In each case, the 50 nm titanium layer was deposited first using a 50 W power setting and 15 standard cubic centimeter per minute (sccm) argon flow rate. Then the 200 nm gold layer was deposited using a 35 W setting to start the plasma interactions and

a 25 W setting during the sputtering. Again with the gold, the argon flow rate was set at 15 sccm. The gold was applied by attempting 1000 angstroms or (100 nm) at a time.

After the metal deposits, the remaining photoresist is then removed (during liftoff). As the photoresist is removed the metal on top of the photoresist is also removed. Just as mentioned in section 4.2, the photoresist is removed just as if one were cleaning all the photoresist off for another photolithography attempt. This removal is done by applying acetone and IPA with a thorough rinse of ultra-pure water. It was also mentioned in section 4.2 that the desired ratio of photoresist thickness to metal thickness is approximately 10:1. This is desired so that the process of liftoff may occur more effectively. It is also desired that the photoresist have a slight beveled angle at the substrate so that the acetone is more readily able to reach the bottom of the photoresist.
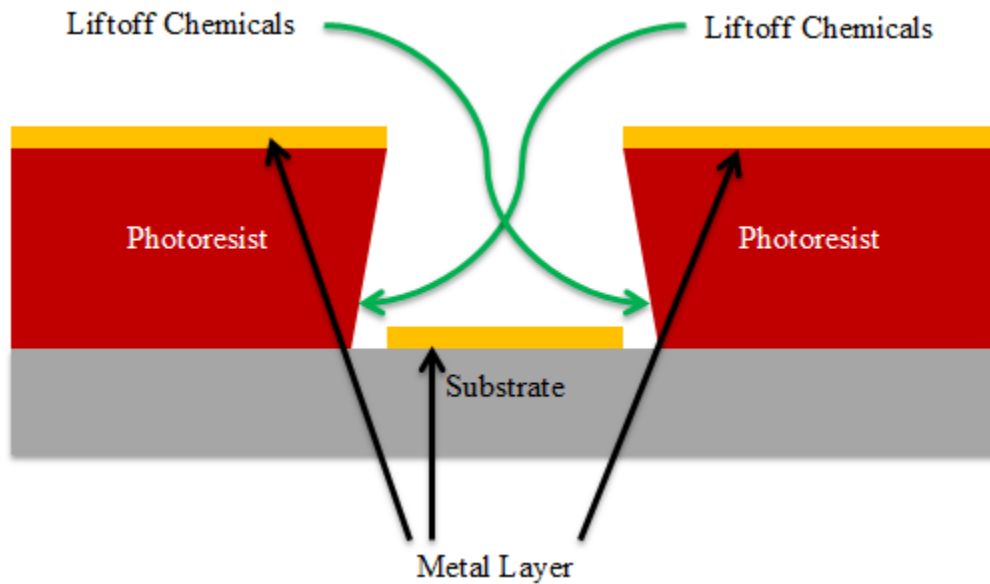
Figure 4.3 - Optimal Liftoff Scenario

This combination of metallization and liftoff was the most challenging hurdle in the fabrication process. In the first attempt, the liftoff process removed the gold layer from the substrate in addition to photoresist. However, it appeared the titanium layer remained. It is theorized that the oxidation of the titanium during the switching of targets in the sputtering machine prevented the gold from properly adhering. A second attempt was planned to address this issue. In order to make a new attempt, the LT-GaAs must be cleaned to remove the remaining titanium. Unfortunately, an improper cleaning solution was used. The wafer was cleaned using RCA-2 which removes metallic residues. It is commonly used under these conditions with silicon substrates; however, it is not suitable for GaAs. RCA-2 is 6 parts H_2O (DI Water) to 1 part HCl_2 (Hydrochloric Acid) to 1 part H_2O_2 (Hydrogen Peroxide) and unfortunately etches GaAs. Therefore the process damaged the wafer beyond use. New substrates without the low temperature layer were purchased. It was believed that these substrates would function for the THz system transmitter but not the receiver since short carrier lifetimes are only required on the detection antenna. Therefore, the commercially available THz antenna illustrated in Figure 4.1 was also purchased to use as a receiver.

In the second sputtering attempt, the issue of titanium oxidation was addressed by altering the way the targets were changed during sputtering. The small sputtering machine used only allows one target at a time. Therefore, in order to switch from titanium to gold, the vacuum on the chamber must be released and the cover opened. This subjects the substrate to open air. In order to overcome this challenge, the chamber was flooded with nitrogen (Ni) during the exchange of targets. In addition, this exchange was done as quickly as possible by an experienced user. All other variables remained the

same since the titanium appeared to adhere on the earlier attempt. Additional steps were taken during lift off to allow maximum chance for success. Instead of using a sonic cleaner to apply the acetone to the covered substrate, the substrate was allowed to sit in calm acetone on a hot plate set at 60^oC for tens of hours with occasional swishing. Although some photoresist area had begun to lift off, the process was taking too long and a new approach was attempted. The least intrusive way to remove the remaining photoresist and subsequent unwanted metal layers was to use extended time in the plasma ash. The substrate was put in plasma ash for no more than 6 minutes at time repeatedly so that the substrate would not experience unwanted thermal stress. This was continued until no further progress was observed. After this attempt, approximately 20% of the antennas looked usable under the microscope. The other 80% either did not adhere properly or had remaining undesired metal leading to possible interconnections. It was also noted that this time the adherence problem was not between the titanium and the gold but between the titanium and the substrate. Unfortunately, as the wafer went through subsequent processing in the form of dicing, cleaving, and embedding onto a printed circuit board, it was observed that the suspected good antenna structures either were damaged or failed to adhere.

For the third attempt, additional steps were taken to solve the problem of adherence. This time, the same quick exchange of targets and minimizing of oxygen in the chamber during the switch were performed. In addition, an additional cleaning of the wafer before the sputtering was performed. The wafer was placed in an ammonium hydroxide bath consisting of 1 part NH_4OH and 10 parts ultra-pure H_2O (UPW) for 60 seconds followed by a 60 second UPW rinse. This method was chosen because it is

known to remove gallium oxides and photoresist scum. A modified RCA1 cleaning of

5:2:50 $NH_4OH:H_2O_2$:distilled H_2O for 60 seconds followed by a 60 second UPW rinse

was considered but rejected because although it is more effective in removal of

photoresist scum, it is known to slightly etch GaAs and leave oxides. With these

additional steps, the antenna yield improved to approximately 50%. The samples were

cleaved and embedded in PCBs. However, even though the adherence was significantly

improved, the traces were still not adhering adequately for wire bonding (see section 4.5).

Some examples of the most successful antennas are shown in Figure 4.4, Figure 4.5, and

Figure 4.6.

Figure 4.4 - Picture of Fabricated Bowtie with Full Coplanar Line Separation
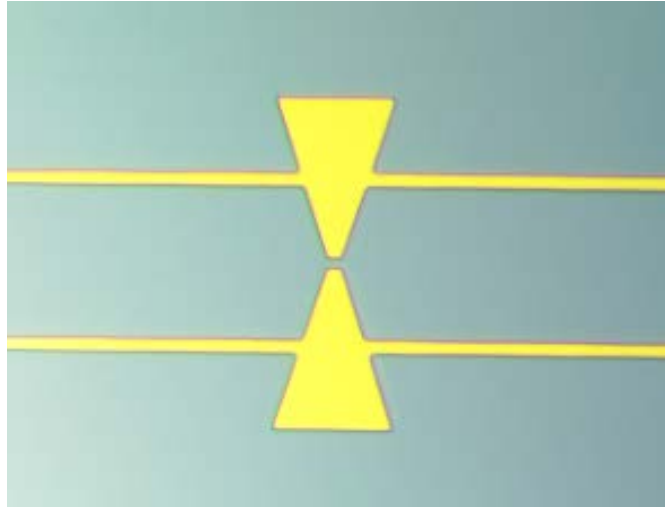
Figure 4.5 - Picture of Fabricated Bowtie with Half Coplanar Line Separation
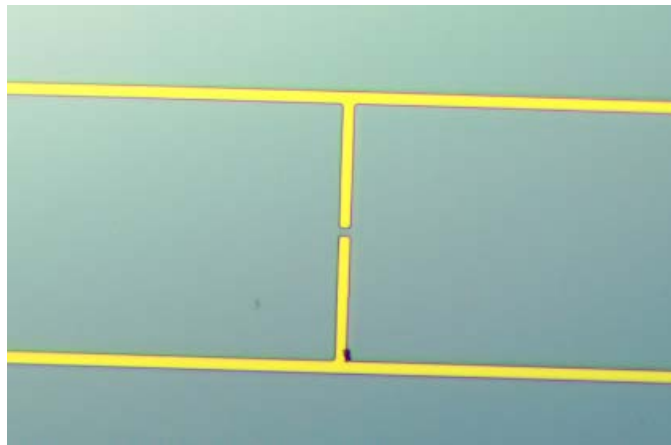
Figure 4.6 - Picture of Fabricated Dipole with Full Coplanar Separation

Subsequent attempts will be made with other metallization approaches. The next attempts will utilize electron beam evaporation at the recommendation of Dr. Hastings, University of Kentucky. This is a more commonly used approach for GaAs processing. In electron beam evaporation, the target anode is bombarded by an electron beam from a charged filament under vacuum. This beam transforms the target atoms into a gaseous

73

phase. These atoms then precipitate on the desired substrate. This method adds the benefits of more directional application of the metal (line of sight) and increased wear resistance.

4.4 Cleaving and Dicing

After the metal traces are applied to the substrate, it must be cut into the desired pieces for real application. This is achieved using either dicing or cleaving. All of the wafers used in this experiment have a [100] orientation. This means that molecular structure of the wafer is such that it should easily separate along lattice lines in the vertical and horizontal normal directions. Therefore, the blocks to be separated are placed with "streets" for cutting in the horizontal and vertical directions (see Figure 4.2). The first attempt of separating the wafer along the "cleave lines" or "streets" was first attempted using dicing. Dicing uses a fine diamond tipped saw to cut the wafer as desired. However, the specific dicing machine used did not handle manipulation of the wafer between cuts well and much of the wafer was broken in undesired places. The dicing process was ceased and the remaining "cuts" were accomplished using cleaving.

With cleaving, the wafer is etched with a diamond scribe along the desired break line. Gentle even pressure is applied such that the wafer breaks or "cleaves" along the desired line. This method proved to be very successful with no undesired results. Therefore, it was used for all later separations of the wafer.

4.5   Embedding on Printed Circuit Boards

Finally, in order to supply voltage biases to the antenna coplanar lines and make the

desired current measurements on the receiver, these antenna structures must have

connections to the necessary equipment. The same antenna holder used with the

commercial THz transmit antenna was to be used for the fabricated antennas. Therefore,

printed circuit boards using the same form factor were created. The antenna holder is the

T8-H2 Alignment Package from Thorlabs, Inc./Menlo.
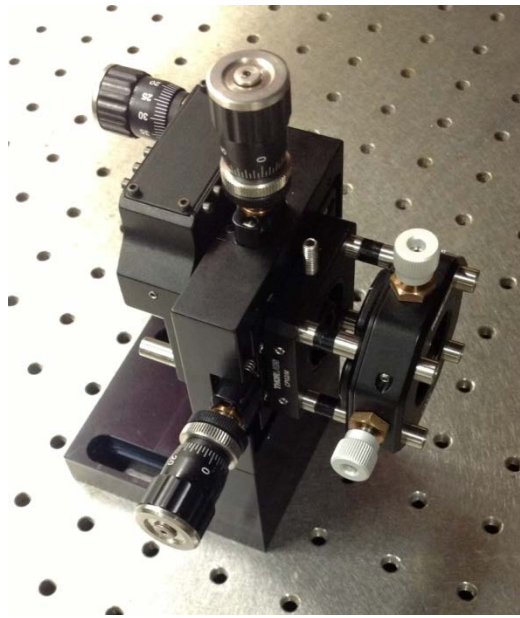
Figure 4.7 - Picture of T8-H2 Alignment Package

It is designed for use with the antenna in Figure 4.1. This antenna has the general

form factor described in Figure 4.8 with the antenna gap designed to be placed in the

center of the four mounting holes.
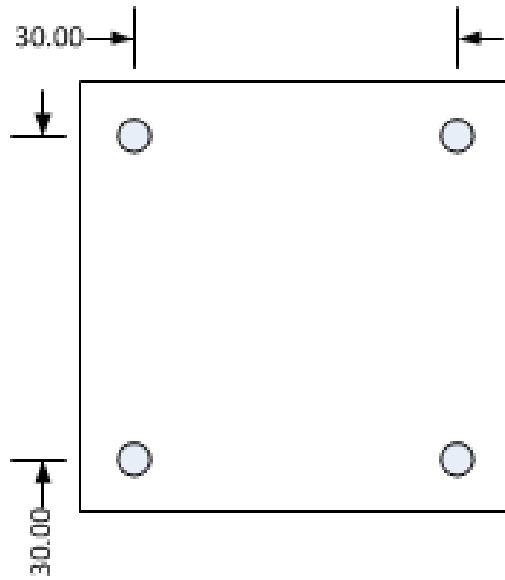
Figure 4.8 - Menlo THz Antenna Form Factor

The fabricated antennas are placed on wafer pieces such that they are situated in

two columns and varying amounts of rows as in Figure 4.9.
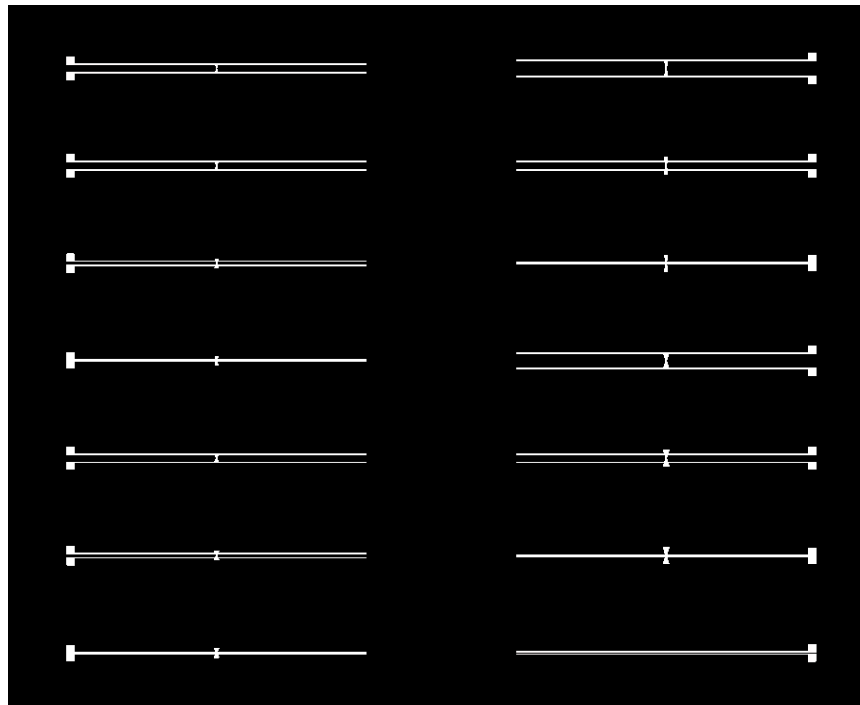
Figure 4.9 - Sample Wafer Block

In this manner a high number of antennas can be fabricated and tested with a limited number of boards.   The printed circuit test boards are made so that they can fit the mounting posts of the holder but also be maneuvered to focus the laser pulse on the different antennas. This is accomplished by changing the post holes to sliders and created two sets, one for each column of antennas (see Figure 4.10).
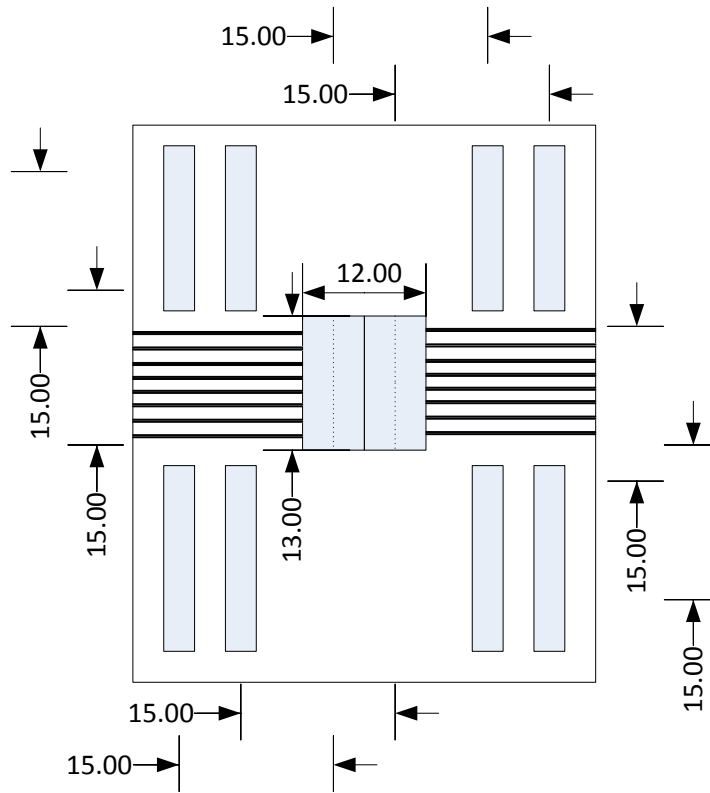
Figure 4.10 - Printed Circuit Board General Design

The wafer blocks are epoxied to the rear of the boards such that the laser pulse can be directed at the gap through the hole in the board. This will allow the THz radiation to be emitter out the back of the wafer (see Figure 4.11).
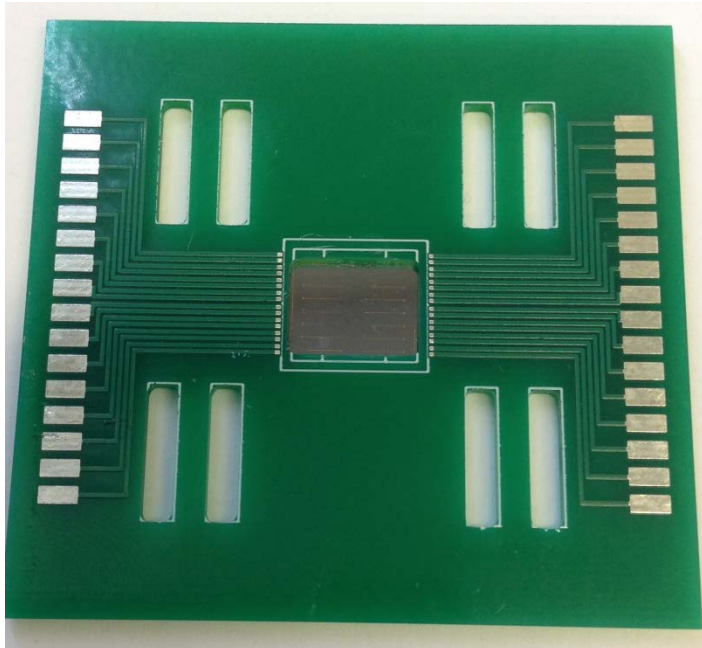
Figure 4.11 - Full Board Picture

Since the current antenna traces did not adhere strong enough for wire bonding, six antennas (3 different designs on two different boards) are connected to the PCB by wire bonding one end of a wire to the PCB and connecting the other end to the antenna pads via conductive paste. Although, not ideal, this connection is sufficient for preliminary testing (see Section 5). Wires are then soldered to the pads on the PCB so that connections to the necessary equipment can be made. Two completed boards are illustrated in Figure 4.12 and Figure 4.13.
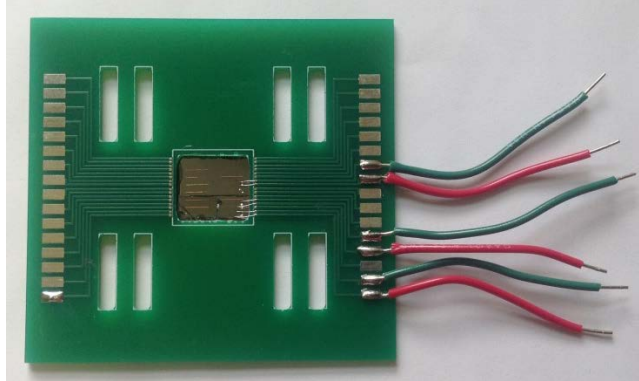
Figure 4.12 - Finished Antenna Set A
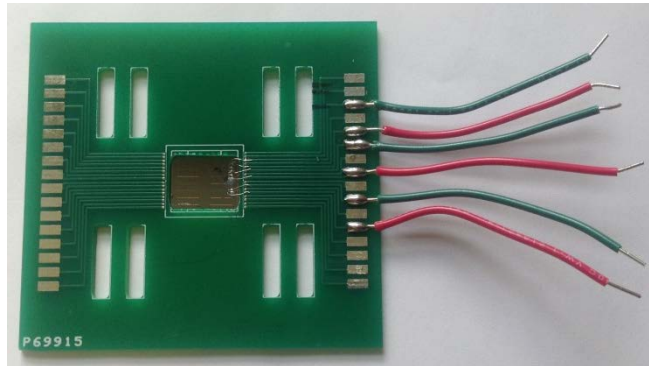
Figure 4.13 - Finished Antenna Set B

5   TESTING

5.1   Testing Approach and Goals

Terahertz waves can be generated by exciting a voltage-biased antenna placed on a photoconductive semiconductor wafer with an extremely short laser pulse [2]. The pulsed laser generates charge carriers in the substrate which are swept onto the metallic antenna traces to produce an electric current that radiates a terahertz band signal. The laser pulse on the emitter is referred to as the pump pulse. A similar approach is used for detection where the voltage bias is not needed. Instead the charge carriers generated by the laser pulse are moved by the incoming signal radiated from the transmitter. This charge carrier movement similarly produces an electric current. The laser pulse on the detector is referred to as the probe pulse.

This method is used to conduct experiments using the fabricated antennas in Chapter 4. The goal of this experiment is to measure the current in the detector antenna in the presence of the incident THz wave. By varying the time delay between the pump and probe pulses, the time dependent amplitude of the THz radiation is measured. The frequency response of the THz radiation is then deduced using a Fourier transform [25].

5.2   Current vs. Voltage Curves

First, the connectivity and functionality of the antennas is tested by investigating the current-voltage relationship of the substrate through the connections on the PCB. The substrate is expected to function as a resistor in the absence of photogeneration. This is

confirmed by measuring the dark current (or current in the absence of photogeneration) at varying bias voltages. The bias voltage is applied across the antenna gap by connecting the leads from the PC board that connect to the coplanar lines of the antenna to a voltage source. The current through the antenna is then measured at varying supply voltages from 1V to 35V. The current-voltage relationships of the six successfully fabricated antennas are found in Figure 5.1.
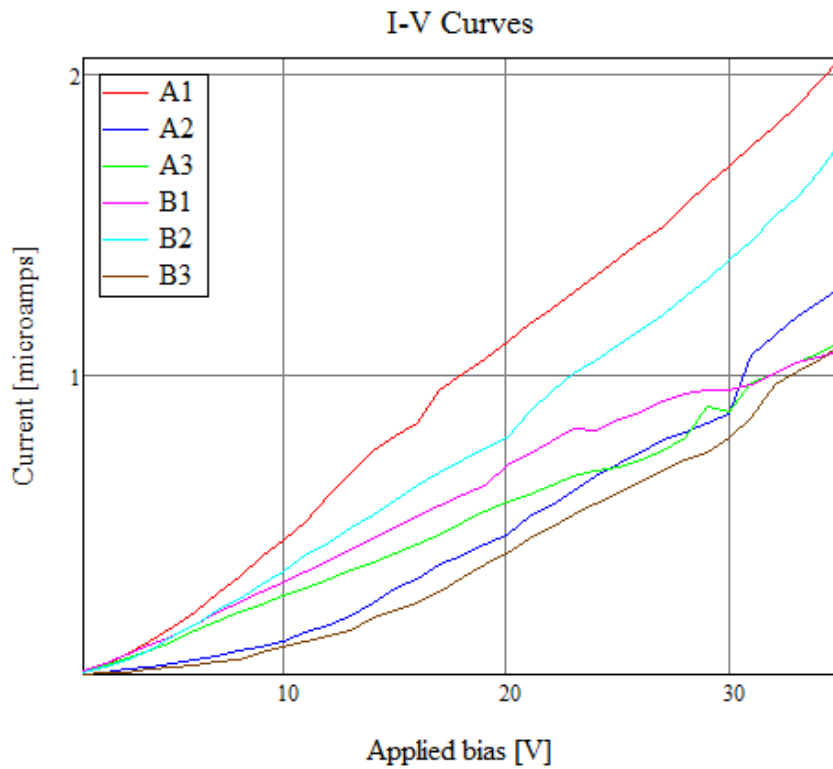
Figure 5.1 - Antenna Current vs. Voltage Curves

5.3   Equipment Setup and Specifications

THz radiation experiments are conducted using the approach described in Section 5.1 using the facilities at the Ultrafast Spectroscopy Lab at the University of Louisville.

A Ti:Sapphire laser with < 150 fs laser pulse at 775 nm is used to supply the pump and probe pulses. A manual delay stage is used to set an initial delay for the probe pulse to compensate for the transmission time of the emitted THz wave. A motorized delay stage and lock in amplifier are used to record the time-dependent current intensities. Figure 5.2 is a diagram of the experiment setup.
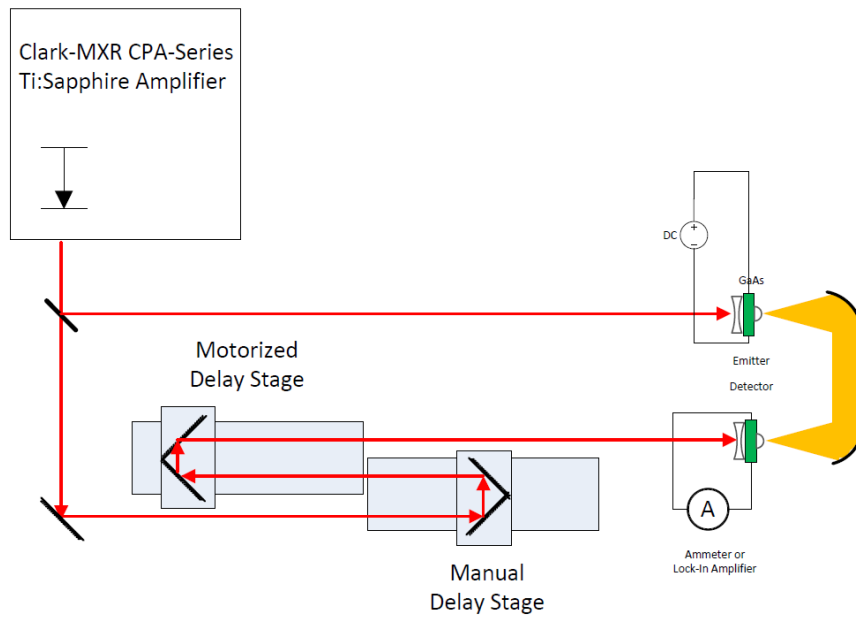
Figure 5.2 - THz Spectroscopy System Setup

The emitter and detector antennas are mounted in the T8-H2 alignment package holders with a focusing lens directing the laser beam on one side and a silica lens collimating the radiated wave for maximum efficiency. Parabolic mirrors are used to direct the THz wave from the emitter to the detector. Figure 5.3 and Figure 5.4 show a closer schematic and demonstration picture of the transmission portion of the setup.
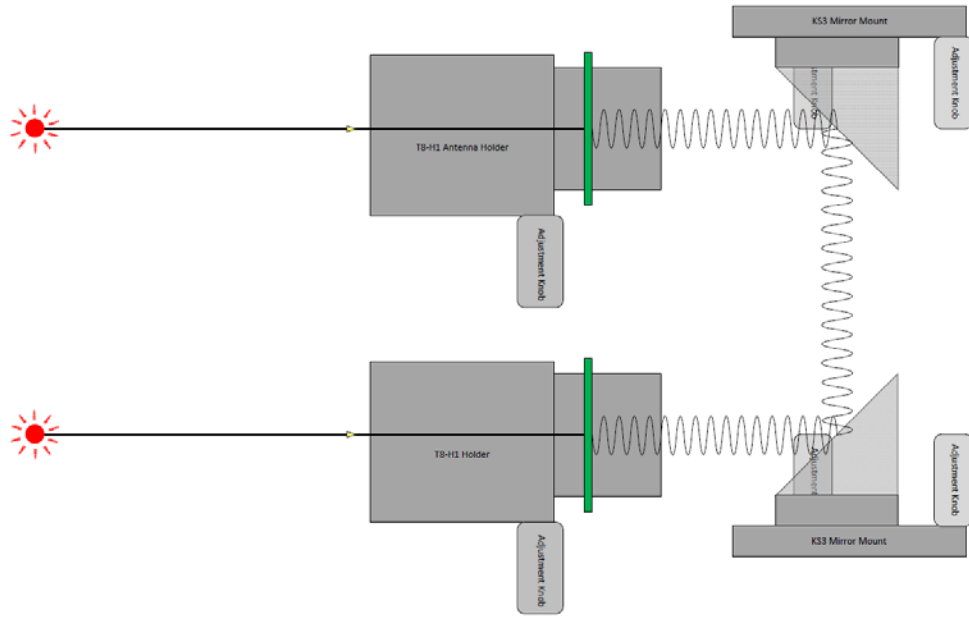
Figure 5.3 - THz Transmission Diagram
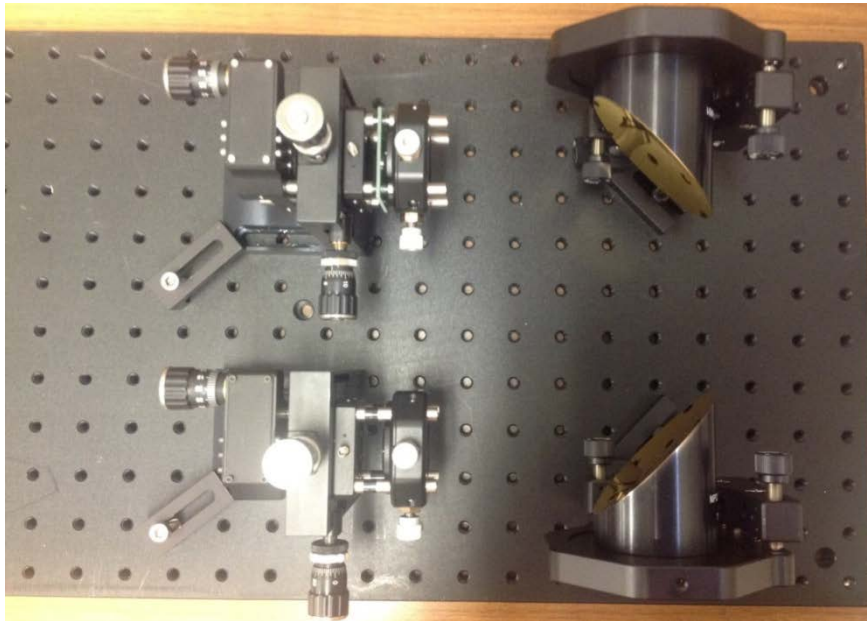
Figure 5.4 - Test Demonstration Setup

To maximize the signal on the detector, the transmission portion of the testing setup is isolated from normal atmospheric conditions by purging the atmosphere in the area. The purge box in Figure 5.5 is used with a flow valve to continually flood the testing area with nitrogen during the experiment.

Figure 5.5 - Purge Box

5.4   Results

Multiple attempts were made with various combinations of emitter and detector antenna using the commercial purchased antenna and the six fabricated antennas. Although it is believed that some interaction between the emitter and detector was detected on occasion, successful measurements were not achieved. Various voltage biases were attempted. Many focusing attempts were made with and without the focusing lenses to place the beam spot on the dipole gap. Measurements were attempted using the ammeter and the lock-in amplifier directly.

Unfortunately, all our antennas were either burned up or damaged during the testing with no valid results recorded. The laser and lab equipment used was at least 10,000 times too powerful. The commercial antenna datasheet lists a maximum optical pulse energy of 0.1 nJ. It recommends < 10mW of optical pulse power with around 100 MHz repetition rate and a < 100 fs pulse. Therefore, the optical pulse energy

$$E = \frac{P_{pulse}}{Rate_{repetition}} = \frac{10mW}{100 \times 10^6 \, Hz} = 0.1nJ \, . \tag{5.1}$$

However, the laser system used had an optical pulse power around 10-40 mW, a pulse duration of < 150 fs, but a 1 kH repetition rate. Therefore, the optical pulse energy can be approximated by

$$E = \frac{P_{pulse}}{Rate_{repetition}} = \frac{10mW}{10^3 \, Hz} = 10\mu J \, . \tag{5.2}$$

The much more powerful optical pulse energy scorched the antenna and substrate beyond use. The fabricated antennas were also damaged in similar fashion. It is assumed that the fabricated antenna have similar damage thresholds as the commercial antenna. Further testing will require a laser system with a much higher repetition rate or lower optical pulse energy. The burned antennas are shown in Figure 5.6, Figure 5.7, Figure 5.8, Figure 5.9, and Figure 5.10.
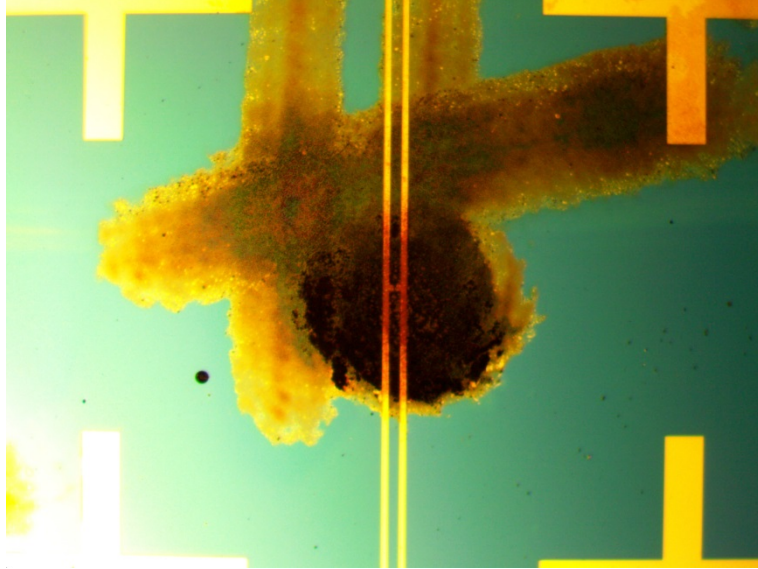
Figure 5.6 - Damaged Commercial Antenna
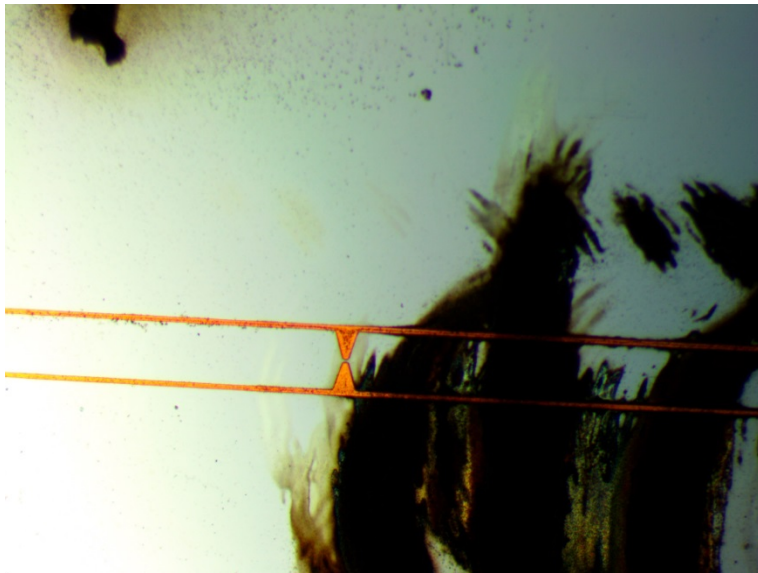
Figure 5.7 - Damaged Fabricated Antenna 1
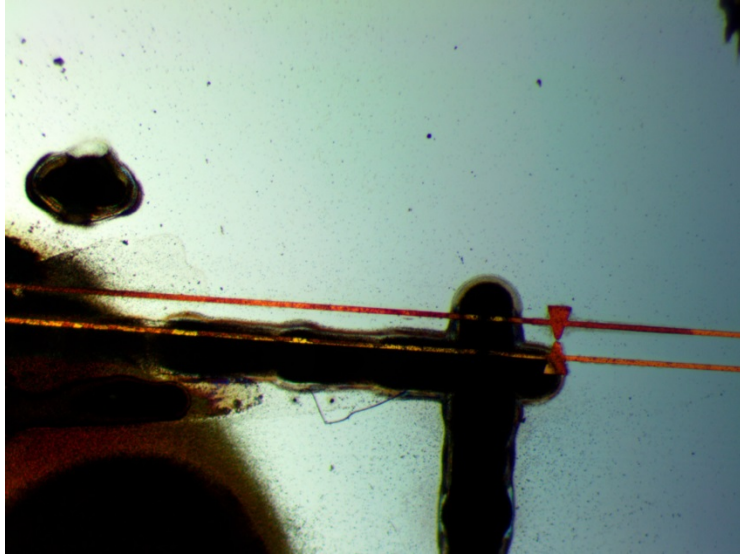
Figure 5.8 - Damaged Fabricated Antenna 2
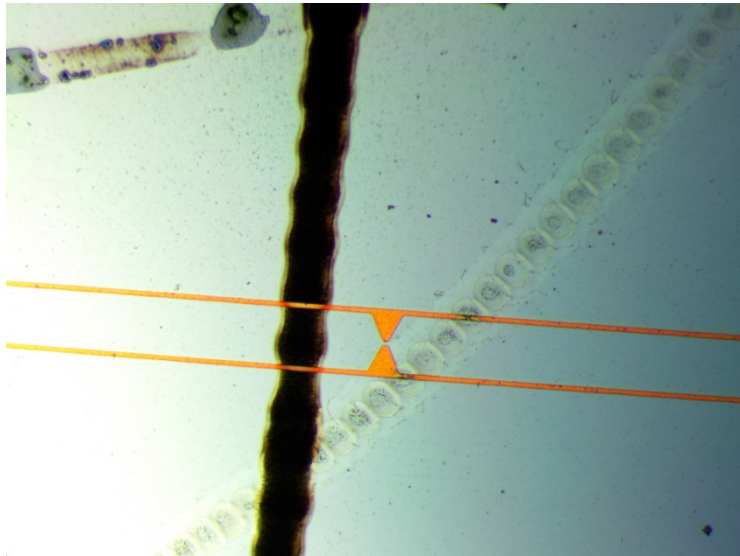
Figure 5.9 - Damaged Fabricated Antenna 3
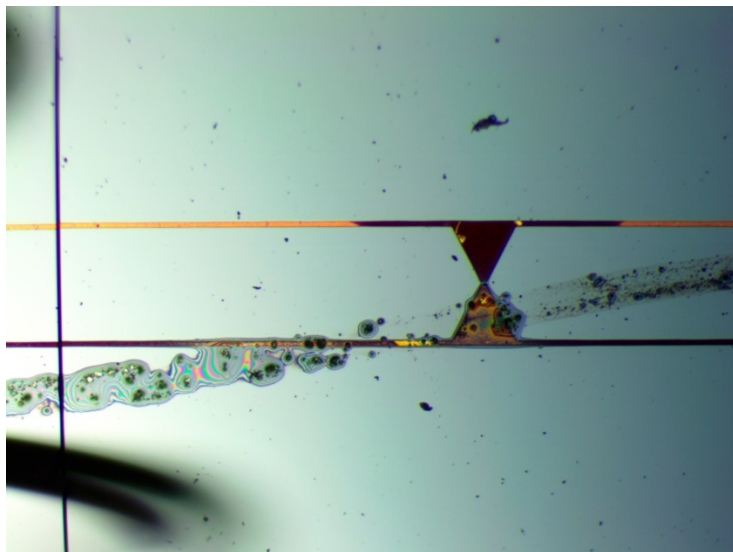
Figure 5.10 - Damaged Fabricated Antenna 4

In addition to the damage from the laser, the additional antenna suffered cracks between the dipole and the pads. These cracks occurred while manipulating the antenna during testing. Figure 5.10, Figure 5.11, Figure 5.12 show the cracks in the coplanar lines.
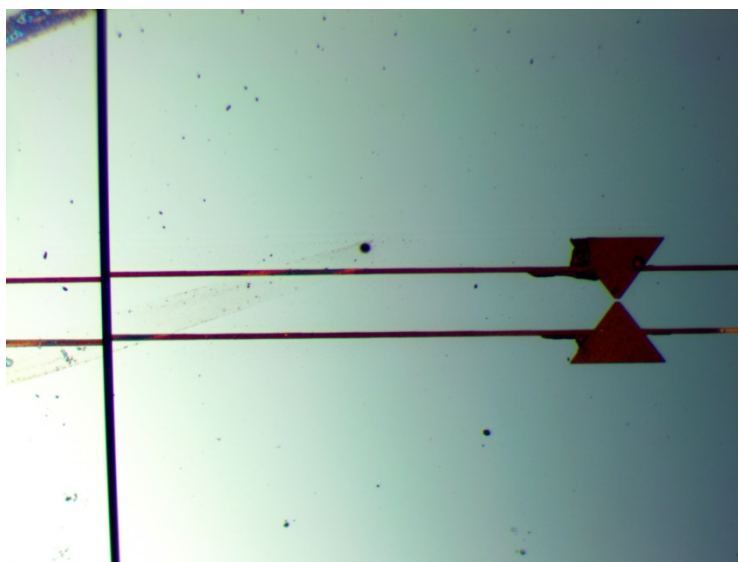
Figure 5.11 - Damaged Fabricated Antenna 5
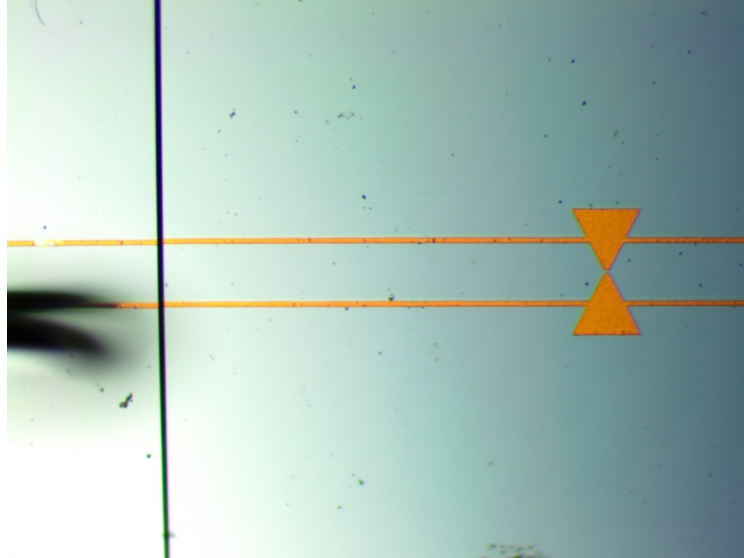
Figure 5.12 - Damaged Fabricated Antenna 6

Finally, Takehito Suzuki at the Ibaraki University was able to print traces on some LT-GaAs and SI-GaAs wafers and conduct some testing of several bowtie antennas (see Chapter 3.4 for more information). The antennas are illustrated in Figure 5.13 and Figure 5.14.
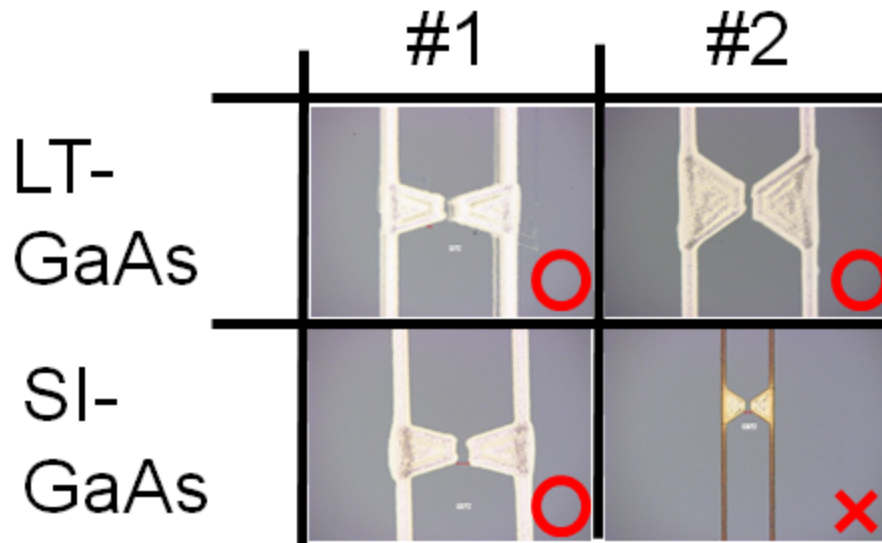
Figure 5.13 - Suzuki Fabricated Full Coplanar Line Separation Bowtie Antennas[26]
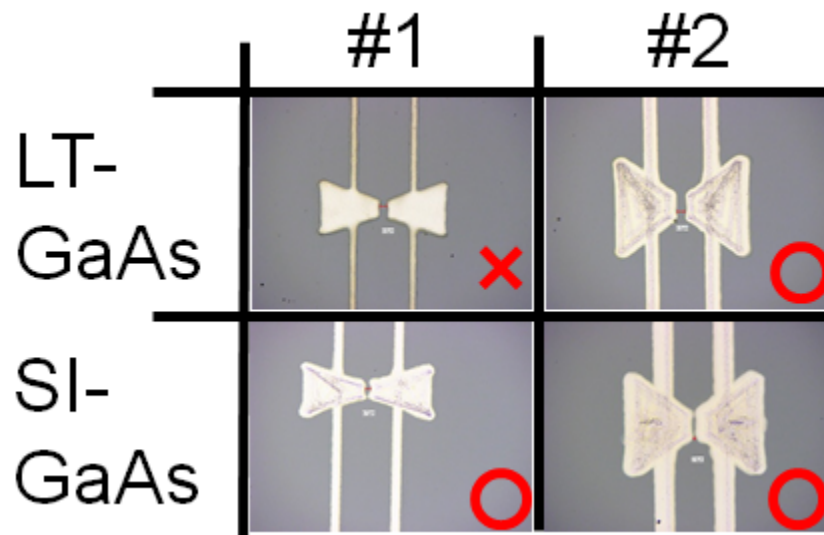
Figure 5.14 - Suzuki Fabricated Half Coplanar Line Separation Bowtie Antennas[26]

6   CONCLUSIONS

In conclusion, in this thesis the coupling of Maxwell's equations and the semiconductor physics equations governing the functionality of the THz photoconductive antenna were presented. A solution of the coupled set of equations via a Discontinuous Galerkin Finite Element Time Domain (DGFETD) method was also presented. A port implementation of the semiconductor interactions with the excitation laser was used for the proposed formulation.

The DGFETD method was validated through the simulation of a number of photoconductive THz antenna devices, including double sided dipole, bowtie, and split-ring resonator antenna structures. The simulated results were validated through comparison with experimental data from publications and testing. Interesting characteristics of the antenna design were illustrated including, but not limited to, the shifting of resonant frequency due to the placement of the coplanar lines, the flattening of the emission intensity response by the use of bowtie geometry, the amplification of peak intensities due to the addition of a second ring in the split-ring resonator structures, and the effects of gap placement in the split-ring resonators.

Fabrication of devices was competed using photolithography, application of traces, liftoff, cleaving, and embedding into printed circuit boards. During this process, faulty attempts were encountered. More successful methods were identified and evaluated. More specifically, cleaning the wafer thoroughly with oxygen plasma ashing and an ammonium hydroxide bath with an ultra-pure water rinse and minimizing the exposure of

the wafer and traces to air between changing the trace materials during sputtering yielded the best results.

The functionality of these devices was demonstrated with the measurement of dark current vs. voltage bias. Spectroscopy testing was conducted and challenges were identified and evaluated. Specifications for further testing were presented. Successful printing and testing of devices was accomplished via a partnership with Taketo Suzuki, et al.

In summary, the DGFETD method coupled with photoconductive antenna device physics was validated and used to evaluate various antenna structures. A road map for successful fabrication and testing of photoconductive antennas on a LT-GaAs substrate was also presented.

7   REFERENCES

[1]   P. H. Siegel, "Terahertz technology," *IEEE Transactions on Microwave Theory and Techniques,* vol. 50, pp. 910-928, Mar 2002.

[2]   P. U. Jepsen, R. H. Jacobsen, and S. R. Keiding, "Generation and detection of terahertz pulses from biased semiconductor antennas," *Journal of the Optical Society of America B-Optical Physics,* vol. 13, pp. 2424-2436, Nov 1996.

[3]   W. C. Gibson, *The method of moments in electromagnetics*. Boca Raton: Chapman & Hall/CRC, 2008.

[4]   J. C. Young, T. Suzuki, D. Boyd, and S. D. Gedney, "A DGFETD Analysis of a Terahertz-Band Photoconductive Dipole Antenna," unpublished|.

[5]   J. S. Hesthaven and T. Warburton, "High-order nodal discontinuous Galerkin methods for the Maxwell eigenvalue problem," *Philosophical Transactions of the Royal Society of London Series a-Mathematical Physical and Engineering Sciences,* vol. 362, pp. 493-524, Mar 15 2004.

[6]   K. S. Yee, "Numerical Solution of Initial Boundary Value Problems Involving Maxwells Equations in Isotropic Media," *IEEE Transactions on Antennas and Propagation,* vol. Ap14, pp. 302-&, 1966.

[7]   S. D. Gedney, *Introduction to the Finite-Difference Time-Domain (FDTD) Method for Electromagnetics*. Lexington, KY: Morgan & Claypool Publishers, 2011.

[8]   F. L. Teixeira, "Time-domain finite-difference and finite-element methods for Maxwell equations in complex media," *IEEE Transactions on Antennas and Propagation,* vol. 56, pp. 2150-2166, Aug 2008.

[9]   S. D. Gedney, C. Luo, J. A. Roden, R. D. Crawford, B. Guernsey, J. A. Miller, T. Kramer, and E. W. Lucas, "The Discontinuous Galerkin Finite-Element Time-Domain Method Solution of Maxwell's Equations," *Applied Computational Electromagnetics Society Journal,* vol. 24, pp. 129-142, Apr 2009.

[10]   C. L. S. Gedney, B. Guernsey, J. A. Roden, R. Crawford, and J. A. Miller, "The Discontinuous Galerkin Finite-Element Time-Domain Method (DGFETD): A High Order, Globally-Explicit Method for Parallel Computation," in *IEEE International Symposium on Electromagnetic Compatibility*, Honolulu, HI, 2007.

[11]   D. K. Sun, J. F. Lee, and Z. Cendes, "Construction of nearly orthogonal Nedelec bases for rapid convergence with multilevel preconditioned solvers," *Siam Journal on Scientific Computing,* vol. 23, pp. 1053-1076, Dec 18 2001.

[12]   J. P. Webb, "Hierarchal vector basis functions of arbitrary order for triangular and tetrahedral finite elements," *IEEE Transactions on Antennas and Propagation,* vol. 47, pp. 1244-1253, Aug 1999.

[13]   P. Fernandes and M. Raffetto, "Characterization of spurious-free finite element methods in electromagnetics," *Compel-the International Journal for Computation*

and Mathematics in Electrical and Electronic Engineering, vol. 21, pp. 147-164, 2002.

[14] J. S. Hesthaven and T. Warburton, "High-order accurate methods for time-domain electromagnetics," *CMES-Computer Modeling in Engineering & Sciences,* vol. 5, pp. 395-407, May 2004.

[15] S. D. Gedney, J. C. Young, T. C. Kramer, and J. A. Roden, "A Discontinuous Galerkin Finite Element Time-Domain Method Modeling of Dispersive Media," *IEEE Transactions on Antennas and Propagation,* vol. 60, pp. 1969-1977, Apr 2012.

[16] Z. Bo, "Deriving the DGFETD with a Riemann Solution," unpublished.

[17] M. H. Chen, B. Cockburn, and F. Reitich, "High-order RKDG methods for computational electromagnetics," *Journal of Scientific Computing,* vol. 22-3, pp. 205-226, Jan 2005.

[18] S. Gottlieb, C. W. Shu, and E. Tadmor, "Strong stability-preserving high-order time discretization methods," *Siam Review,* vol. 43, pp. 89-112, Mar 2001.

[19] R. F. Pierret, *Advanced semiconductor fundamentals*, 2nd ed. Upper Saddle River, N.J.: Prentice Hall, 2003.

[20] R. F. Pierret, *Advanced semiconductor fundamentals*. Reading, Mass.: Addison-Wesley Pub. Co., 1987.

[21] J. C. Young, "pc_antenna_v6.doc," unpublished, 2013.

[22] J. C. Young, D. Boyd, S. D. Gedney, J. Liu, and T. Suzuki, "A Comparison of Measured and Computed Data for Photoconductive Antennas," in *Antennas and Propagation and USNC-URSI National Radio Science Meeting*, Orlando, FL, 2013.

[23] P. Kirawanich, "A full wave analysis of a terahertz-pulse generation for wide-bandgap photoconductive antennas using a field-carrier transport scheme " presented at the ECTI-CON 2009 6th International Conference, 2009.

[24] E. Sano, "A Device Model for Metal-Semiconductor Metal Photodetectors and Its Applications to Optoelectronic Integrated-Circuit Simulation," *IEEE Transactions on Electron Devices,* vol. 37, pp. 1964-1968, Sep 1990.

[25] F. Miyamaru, Y. Saito, K. Yamamoto, T. Furuya, S. Nishizawa, and M. Tani, "Dependence of emission of terahertz radiation on geometrical parameters of dipole photoconductive antennas," *Applied Physics Letters,* vol. 96, May 24 2010.

[26] N. S. Koja, Takehito, "John-san's Photoconductive Antenna,", unpublished, 2014, p. 7.

[27] K. Takano, Y. Chiyoda, T. Nishida, F. Miyamaru, T. Kawabata, H. Sasaki, M. W. Takeda, and M. Hangyo, "Optical switching of terahertz radiation from meta-atom-loaded photoconductive antennas," *Applied Physics Letters,* vol. 99, Oct 17 2011.

[28] Z. Jaksic, O. Jaksic, Z. Djuric, and C. Kment, "A consideration of the use of metamaterials for sensing applications: field fluctuations and ultimate performance," *Journal of Optics a-Pure and Applied Optics,* vol. 9, pp. S377-S384, Sep 2007.

[29]   J. B. Pendry, A. J. Holden, D. J. Robbins, and W. J. Stewart, "Magnetism from conductors and enhanced nonlinear phenomena," *IEEE Transactions on Microwave Theory and Techniques,* vol. 47, pp. 2075-2084, Nov 1999.

[30]   D. R. Smith, W. J. Padilla, D. C. Vier, S. C. Nemat-Nasser, and S. Schultz, "Composite medium with simultaneously negative permeability and permittivity," *Physical Review Letters,* vol. 84, pp. 4184-4187, May 1, 2000.

[31]   S. Gupta, J. F. Whitaker, and G. A. Mourou, "Ultrafast Carrier Dynamics in Iii-V-Semiconductors Grown by Molecular-Beam Epitaxy at Very Low Substrate Temperatures," *IEEE Journal of Quantum Electronics,* vol. 28, pp. 2464-2472, Oct 1992.

[32]   D. C. Look, "On Compensation and Conductivity Models for Molecular-Beam-Epitaxial Gaas Grown at Low-Temperature," *Journal of Applied Physics,* vol. 70, pp. 3148-3151, Sep 15 1991.

[33]   L.E. Kingsley, "A Study of Picosecond, High-Voltage Photoconductive Switching Using Electro-Optic Diagnostics and Computer-Aided Analysis", pp. 20.

[34]   W. Shi, L. Hou, and X. M. Wang, "High effective terahertz radiation from semi-insulating-GaAs photoconductive antennas with ohmic contact electrodes," *Journal of Applied Physics,* vol. 110, Jul 15 2011.

[35]   N. M. Vieweg, M.; Scheller, M.; Ezdi, K.; Wilk, R.; Hubers, H.-W.; Koch, M., "Enhanced emission from THz antennas made of low-temperature-grown GaAs with annealed ohmic contacts," p. 2, 2009.

[36]   N. Vieweg, M. Mikulics, M. Scheller, K. Ezdi, R. Wilk, H. W. Hubers, and M. Koch, "Impact of the contact metallization on the performance of photoconductive THz antennas," *Optics Express,* vol. 16, pp. 19695-19705, Nov 24 2008.

[37]   G. J. Humpston, D. M., "Gold in Gallium Arsenide Die-Attach Technology," *Gold Bulletin,* vol. 22(3), p. 13, 1989 1989.

8 VITA

EDUCATION

Nazarene Theological Seminary, Kansas City, MO

Master of Divinity, Practical Theology Emphasis, 2003-2007.

The University of Kentucky, Lexington, KY

Bachelor of Science, Electrical Engineering, Business Minor, 1994-1999.

PROFESSIONAL POSITIONS

Research Assistant at the University of Kentucky, Electrical Engineering Department,
Lexington, KY, 2011-2013.

Pastor at Eastland Park Church of the Nazarene, Lexington, KY, 2012-Present, and Oak
Hill Church of the Nazarene, Jacksonville, FL, 2008-2011.

Programmer/Analyst at Nazarene Publishing House, Kansas City, MO, 2004-2009.

Electrical Engineer at the Science Applications International Corp., Hampton, VA,
2002-2004 & 2005-2006.

Electrical Engineering Aerospace Technologist at the National Aeronautics and Space
Administration (NASA) Langley Research Center, Hampton, VA, 1998-2002.

Student Computer Programmer at Kentucky Utilities/Old Dominion Power,
Lexington, KY, 1995-1996.

SCHOLASTIC AND PROFESSIONAL HONORS

 Member of Phi Kappa Phi honor society (2013 - Present).

Ordained Elder in the Church of the Nazarene (2009 - Present).

Nazarene Theological Seminary Honors Program (2003 - 2007).

Nazarene Theological Merit Scholarships (2004 - 2007).

National Aeronautics and Space Administration (NASA) Superior Accomplishment

   Award (2001).

Elk Horn Coal Company Engineering Scholarship (1994 - 1999).

University of Kentucky Merit Scholarship (1995 - 1999).

Member of Eta Kappa Nu electrical engineering honor society (1995 - Present).

Member of Tau Beta Pi engineering honor society (1995 - Present).

Accepted into the University of Kentucky Honors Program (1995).

Served as Engineering Student Council Representative and Public Affairs Officer for the

   University of Kentucky's American Institute of Aeronautics and Astronautics

   Chapter (1997).

Selected for Alpha Lambda Delta freshman honor society (1994).

PROFESSIONAL PUBLICATIONS AND PRESENTATIONS

Young, J.C., Boyd, D.R., Gedney, S.D., Liu, J., & Suzuki, T. (2013, August). A Multi-

   physics Computational Approach to Simulating THz Photoconductive Antennas

   with Comparison to Measured Data and Fabrication of Samples. Poster presented

   at the annual meeting of the Kentucky Innovation & Entrepreneurship

   Conference, Lexington, KY.

Young, J.C., Boyd, D.R., Gedney, S.D., Liu, J., & Suzuki, T. (2013, July). A Comparison

of Measured and Computed Data for Photoconductive Antennas. Presentation

presented at the annual meeting of the IEEE International Symposium on

Antennas and Propagation and USNC-URSI National Radio Science Meeting,

Orlando, FL.